ARL-CR-0765 ● MAR 2015

US Army Research Laboratory

US Army Research Laboratory Materials Center of Excellence

Selected Silicon Carbide Reports from Rutgers Materials Center of Excellence Annual Reports, 2010–2011

edited by JW McCauley (Emeritus)
Cooperative Agreement Manager
Army Research Laboratory
Weapons and Materials Research Directorate
Aberdeen Proving Ground, MD 21005-5066

under contract W911NF-06-2-0007

NOTICES

Disclaimers

The findings in this report are not to be construed as an official Department of the Army position unless so designated by other authorized documents.

Citation of manufacturer's or trade names does not constitute an official endorsement or approval of the use thereof.

Destroy this report when it is no longer needed. Do not return it to the originator.

ARL-CR-0765 ● MAR 2015

US Army Research Laboratory

US Army Research Laboratory Materials Center of Excellence

Selected Silicon Carbide Reports from Rutgers Materials Center of Excellence, 2010–2011

edited by JW McCauley (Emeritus)
Cooperative Agreement Manager
Army Research Laboratory
Weapons and Materials Research Directorate
Aberdeen Proving Ground, MD 21005-5066

under contract W911NF-06-2-0007

REPORT DOCUMENTATION PAGE

Form Approved
OMB No. 0704-0188

1. REPORT DATE *(DD-MM-YYYY)*	2. REPORT TYPE	3. DATES COVERED (From - To)
March 2015	Final	July 2010–June 2011

4. TITLE AND SUBTITLE

US Army Research Laboratory Materials Center of Excellence

Selected Silicon Carbide Reports from Rutgers Materials Center of Excellence Annual Reports, 2010–2011

5a. CONTRACT NUMBER
W911NF-06-2-0007

5b. GRANT NUMBER

5c. PROGRAM ELEMENT NUMBER

6. EDITOR(S)
JW McCauley (Emeritus)

5d. PROJECT NUMBER
BH64

5e. TASK NUMBER

5f. WORK UNIT NUMBER

7. PERFORMING ORGANIZATION NAME(S) AND ADDRESS(ES)
Center for Ceramic Research
Rutgers, The State University of New Jersey
607 Taylor Road
Piscataway, NJ 08854-8065

8. PERFORMING ORGANIZATION REPORT NUMBER
ARL-CR-0765

9. SPONSORING/MONITORING AGENCY NAME(S) AND ADDRESS(ES)
US Army Research Laboratory
ATTN: RDRL-WM
Aberdeen Proving Ground, MD 21005-5069

10. SPONSOR/MONITOR'S ACRONYM(S)
ARL

11. SPONSOR/MONITOR'S REPORT NUMBER(S)

12. DISTRIBUTION/AVAILABILITY STATEMENT
Approved for public release; distribution is unlimited.

13. SUPPLEMENTARY NOTES

14. ABSTRACT

This Materials Cooperative Research Program was conducted as a seamless, synergistic collaboration among the Rutgers Malcolm G. McLaren Center for Ceramic Research and the US Army Research Laboratory's Weapons and Materials Research Directorate to focus the program on substantial improvement and continuous improvement of the scientific and technical understanding of advanced armor ceramics. This report brings together research carried out during 2010–2011 on the following tasks: Theoretical Calculations for Silicon Carbide Stacking Faults and Polytypes and The Study of United States Silicon Carbide Powder Variations.

15. SUBJECT TERMS
silicon carbide, theoretical calculations, powder characterization, polytypes, stacking faults

16. SECURITY CLASSIFICATION OF:			17. LIMITATION OF ABSTRACT	18. NUMBER OF PAGES	19a. NAME OF RESPONSIBLE PERSON
a. REPORT	b. ABSTRACT	c. THIS PAGE			James W McCauley
Unclassified	Unclassified	Unclassified	UU	60	19b. TELEPHONE NUMBER (*Include area code*) 410-306-0711

Standard Form 298 (Rev. 8/98)
Prescribed by ANSI Std. Z39.18

Contents

List of Figures

List of Tables

INTENTIONALLY LEFT BLANK.

1. Introduction

This Materials Cooperative Research Program will be conducted as a seamless, synergistic collaboration among the Rutgers Malcolm G. McLaren Center for Ceramic Research (CCR) and the US Army Research Laboratory's (ARL's) Weapons and Materials Research Directorate. This will enable the program to utilize the capabilities of each organization to focus the program on substantial improvement and continuous improvement of the scientific and technical understanding of advanced armor ceramics.

As part of Year 5 of this program, 5 armor programs within the Ceramic Armor Subgroup of the CCR have been jointly funded within the Cooperative Research Program and 3 additional programs will receive supplemental funding from ARL.

These include:

- Part 1, Task 7: Theoretical Calculations for Silicon Carbide (SiC)
- Part 2, Task 9: Study of United States Silicon Carbide (SiC) Powder Variations

2. Part 1, Task 7: Theoretical Calculations for Silicon Carbide (SiC), Cost Shared with Rutgers University's Ceramic and Composite Materials Center (2010)

Core Faculty: R Haber, DE Niesz

ARL Collaborators: J McCauley, T Jessen

Research Associate: V Domnich

Post Doc: To be determined

2.1 Long-Range Objectives

- Develop a better understanding of the relationship of microstructural characteristics and plastic deformation in silicon carbide (SiC).
- Investigate the effect of additives, starting powders, core-rim structures on polytype distribution, and stacking fault-induced plasticity in SiC.

2.2 Subtasks for Calendar Year 2010

First Quarter Subtasks:

- Using more sophisticated computational capabilities, perform direct calculation polytype stability and stacking fault energies in SiC as a function of pressure, shear stress, and temperature.

Second Quarter Subtasks:

- Using more sophisticated computational capabilities, investigate the effect of additives (aluminum [Al], boron [B], nitrogen [N], and oxygen [O]) on polytype stability and stacking fault mobility in SiC in a range of pressures, shear stresses, and temperatures.

Third Quarter Subtasks:

- Investigate the influence of interfaces between different polytypes on SiC plasticity in a range of pressures, shear stresses, and temperatures.

Fourth Quarter Subtasks:

- Evaluate the role of intrinsic stress/external confinement and the influence of nonrigid grain boundaries on stacking fault dynamics in SiC.

2.3 Background

Because the strength of ceramics is crucial for ballistic performance, assessing the behavior of SiC under dynamic loading has been the subject of numerous studies. SiC has been shown to maintain its strength up to approximately 100 GPa, and it appears to exhibit high degree of ductility above the Hugoniot elastic limit.[1] The exact mechanism for the large plasticity of SiC at higher impact loads is under debate; however, it may be arguably attributed to slippage along the grain boundaries or the formation of large numbers of stacking faults (SFs) in the SiC structure. The SiC stacking fault dynamics at elevated pressures has been studied at Rutgers by Chhowalla and Fanchini (personal communication, 2010, unreferenced). The stacking fault energies (SFEs) have been calculated as a function of pressure for 3C, 4H, and 6H SiC polytypes. It has been demonstrated that the formation of SFs along the basal plane of 6H SiC is more favorable than formation of SFs along any other planes in any other SiC polytype considered. In particular, the onset of SF-induced plasticity in 6H SiC was predicted to occur at approximately 28 GPa, well below a similar onset in the 4H SiC polytype (~67 GPa) or in the 3C SiC polytype (>100 GPa).

Impurities in SiC, the composition of the starting powders, and core-rim effects will all have effects on polytype distribution, SF dynamics, and the resultant plasticity of the material. In this work, we continue the work of Chhowalla and Fanchini and attempt to investigate the effect of additives (Al, B, N, and O) on polytype structure and SF energies in SiC at ambient conditions and at elevated pressures. We will investigate whether additives can promote plastic deformation in SiC in a wider pressure range. The role of intrinsic stress/external confinement and the influence of nonrigid grain boundaries on SF dynamics in SiC polytypes will be addressed. We will also attempt to investigate the influence of interfaces between different polytypes on SiC plasticity in a range of pressures.

2.4 Experimental Approach

All existing SiC polytypes are tetrahedrally bonded and can be seen as an assembly of corner-sharing tetrahedrals (Fig. 2.1). Each tetrahedron *T* consists of 4 Si (C) atoms at its corners bonded to a C (Si) atom at the centroid of the tetrahedron. In the tetrahedron, there is a 3-fold rotational symmetry about each of the 4 Si-C bonds, any of which may be taken as the *c* axis. A 180° rotation about such a direction breaks the 3-fold symmetry and produces a different ("twinned") variant *T′*.[2] The "normal" ("twinned") tetrahedral can occupy 3 different spatial positions

denoted as *T*1, *T*2, and *T*3 (*T*1′, *T*2′, and *T*3′). The SiC polytypes are built up from an assembly of normal (*Ti*) and twinned (*Ti'), i* = 1,2,3, variants with the restriction that any 2 neighboring tetrahedra share a corner.

There are several classification schemes for SiC polytypes. In the common Ramsdell notation, each polytype is characterized as *n*L, where *n* is the periodicity of the tetrahedra along the *c* axis, and L is the symmetry of the resulting structure: L = C for cubic, H for hexagonal, and R for rhombohedral symmetry. In the ABC notation, each basal plane, consisting of only C (Si) atoms, is denoted as A, B, or C depending on the stacking sequences of basal planes along the *c* direction. The Jagodzinski notation reflects difference in configuration of second neighbors on the same sublattice as the site considered and denotes atoms as *k* for cubic-type configuration of second neighbors, like that of atom B in the sequence ABC, and *h* for hexagonal-type configuration of second neighbors, like that of atom B in the sequence ABA. In Hägg notation, (+) is used for AB, BC, and CA stacking sequences, and (−) for BA, CB, and AC stacking sequences. Finally, Zhdanov notation consists of pairs of numbers in which the first number denotes the number of consecutive plus signs and the second the number of consecutive minus signs (Fig. 2.1).

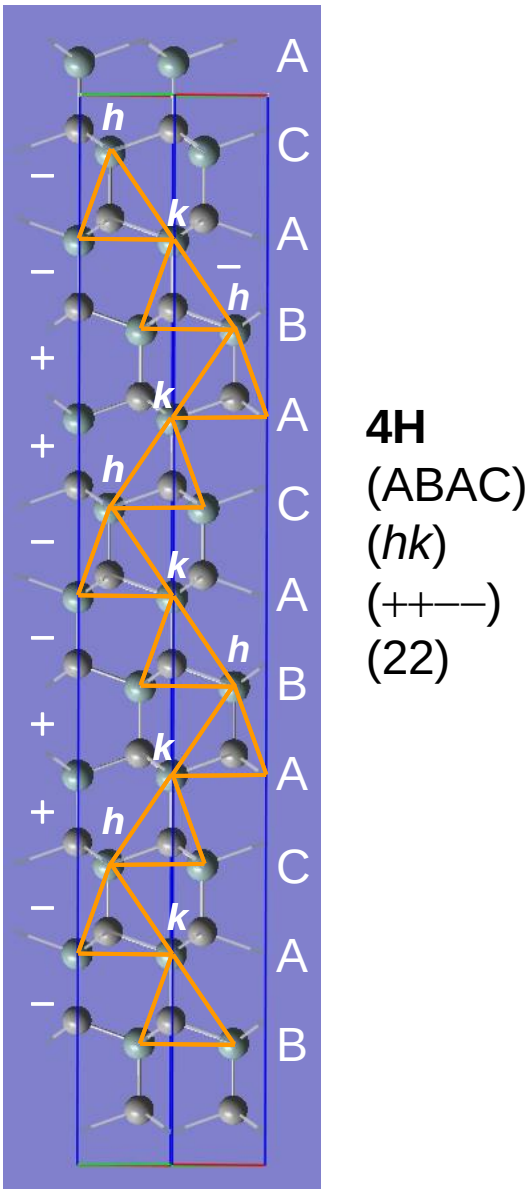

Fig. 2.1 An example of different notations used for SiC polytype classification. The same SiC structure is identified as 4H in Ramsdell notation, (ABAC) in ABC notation, (*hk*) in Jagodzinski notation, (+ + – –) in Hägg notation, and (22) in Zhdanov notation.

Additives in various SiC structures can substitute for Si or C atoms in either *k* or *h* sites. This is illustrated in Fig. 2.2 for the case of the 4H SiC polytype. The available inequivalent substitutional sites in 3C, 2H, 4H, and 6H SiC polytypes are listed in Table 2.1 along with their respective symmetry. N and Al atoms were used as substitutional additives in this study.

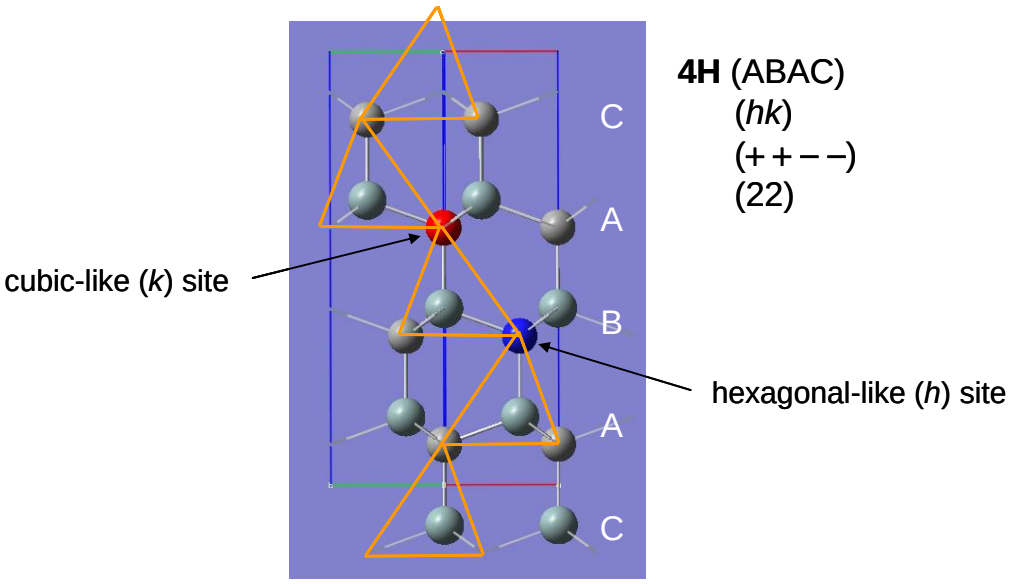

Fig. 2.2 Two inequivalent substitutional sites in 4H SiC, viewed from the [1120] direction. The sites are classified as cubic-like (*k*) and hexagonal-like (*h*) in Jagodzinski notation.

Table 2.1 Inequivalent sites in SiC polytypes[3]

Ramsdell Notation	ABC Notation	Jagodzinski Notation	No. of Inequivalent Si (C) Sites	
			Cubic-like	Hexagonal-like
3C (zincblende)	ABC	*k*	1	0
2H (wurzite)	AB	*h*	0	1
4H	ABAC	*hk*	1	1
6H	ABCACB	*hkk*	2	1

Extended SF regions can be created in SiC by the motion of partial dislocations, leaving behind a faulted crystal containing an error in the stacking sequence. For symmetry reasons, there exists one nondegenerate SF type in 3C SiC, denoted in Zhdanov notation as (111); one nondegenerate SF type in 2H SiC, denoted as (2); 2 nondegenerate SF types in 4H SiC, denoted as (31) and (13); and 3 nondegenerate SF types in 6H SiC, denoted as (42), (24), and (3111).[4] Different types of SFs in SiC polytypes under consideration are illustrated in Fig. 2.3.

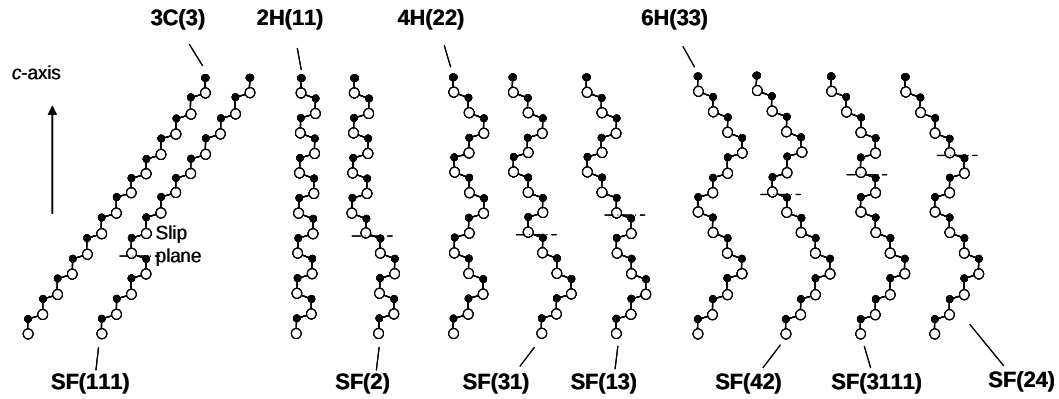

Fig. 2.3 Geometrically distinguishable SFs obtained by glide in 3C, 2H, 4H, and 6H SiC in different slip planes (dashed horizontal lines), viewed from the [1120] direction. SiC polytypes and the corresponding stacking faults are classified following Zhdanov notation.

The SF energy can be defined as[3]

$$\gamma = \frac{E_{faulted} - E_{perfect}}{A}, \tag{1}$$

where A is the interface area, $E_{faulted}$ is the total energy of the crystal with an SF, and $E_{perfect}$ is the total energy of the perfect crystal. In the present approach, the total energy refers to the energy of a supercell, and the area $A = a^2\sqrt{3}/2$ is the area of the supercell in the (0001) basal plane.

The 1-dimensional (1-D) character of the stacking faults in SiC polytypes and the periodic arrangement of the resulting supercells suggests their description with the axial next-nearest-neighbor Ising (ANNNI) model formally identical to the 1-D Ising model for describing the interactions among coupling spins along one crystallographic axis of the lattice.[5] Restricting the interactions to the next-nearest neighbors, the SF energies in this model can be expressed as (with the subscripts on γ denoting polytype and type of SF, respectively).

$$\begin{aligned}
\gamma_{3C(2)} &= \frac{4}{A}\cdot\left(J_1 + J_2 + J_3\right), \\
\gamma_{2H(111)} &= \frac{4}{A}\cdot\left(-J_1 + J_2 - J_3\right), \\
\gamma_{4H(13)} &= \gamma_{4H(31)} = \frac{4}{A}\cdot\left(-J_2\right), \\
\gamma_{6H(24)} &= \gamma_{6H(42)} = \frac{4}{A}\cdot\left(-J_3\right),
\end{aligned} \tag{2}$$

and

$$\gamma_{6H(3111)} = \frac{4}{A}\cdot\left(J_1 - J_2 - J_3\right),$$

where the "spin interaction" energies J can be obtained in terms of the total energies E_{3C}, E_{2H}, E_{4H}, and E_{6H} per Si-C pair in the perfect crystal using much smaller unit cells.

$$\mathrm{J}_1 = \frac{2\mathrm{E}_{2\mathrm{H}} - \mathrm{E}_{3\mathrm{C}} + 2\mathrm{E}_{4\mathrm{H}} - 3\mathrm{E}_{6\mathrm{H}}}{4},$$
$$\mathrm{J}_2 = \frac{-\mathrm{E}_{2\mathrm{H}} - \mathrm{E}_{3\mathrm{C}} + 2\mathrm{E}_{4\mathrm{H}}}{4}, \tag{3}$$

and

$$\mathrm{J}_3 = \frac{-\mathrm{E}_{3\mathrm{C}} - 2\mathrm{E}_{4\mathrm{H}} + 3\mathrm{E}_{6\mathrm{H}}}{4}.$$

The values of E_{3C}, E_{2H}, E_{4H}, and E_{6H} per Si-C pair in the perfect crystal were calculated within the scheme of density-functional theory (DFT) in the local spin density approximation.[6,7] The Slater functional for the exchange energy[8] and the Vosco, Wilk, and Nusair functional for the correlation energy[9] were used. Commercial software (Gaussian) with STO-3G Gaussian-type electronic orbitals[10,11] as the basis set was used in our calculations.

When viewed as a hexagonal structure, 3C SiC has 6 atoms in the primitive unit cell while 2H, 4H, and 6H SiC have 4, 8, and 12 atoms per primitive cell, respectively. To reduce systematic errors during calculation, the total energy minimizations were performed on supercells containing 24 atoms for all polytypes, i.e., the supercells for 3C, 2H, 4H, and 6H SiC consisting of 4, 6, 3, and 2 primitive unit cells stacked on top of one another, respectively.

For the calculation of stacking fault energies at elevated pressures, the exact lattice parameters as a function of pressure need to be calculated. This is achieved by determining elastic constants in SiC polytypes at specific pressure values. To determine elastic constants of a crystal using total energy and force calculations, a deformation of the supercell is imposed by changing the lattice vectors $\overline{R} = \left(\overline{a}, \overline{b}, \overline{c}\right)$ of the undisturbed supercell to $\overline{R'} = \left(\overline{a'}, \overline{b'}, \overline{c'}\right)$ using a strain matrix.[12]

$$\overline{R} = \overline{R'} \begin{pmatrix} 1+e_{xx} & \frac{1}{2}e_{xy} & \frac{1}{2}e_{xz} \\ \frac{1}{2}e_{yx} & 1+e_{yy} & \frac{1}{2}e_{yz} \\ \frac{1}{2}e_{zx} & \frac{1}{2}e_{zy} & 1+e_{zz} \end{pmatrix}. \tag{4}$$

The deformation leads to a change in the total energy of the crystal given by

$$U = \frac{E_{tot} - E_0}{V_0} = \frac{1}{2}\sum_{i=1}^{6}\sum_{j=1}^{6} C_{ij} e_i e_j \,, \tag{5}$$

where E_0 is the total energy of the undisturbed lattice, V_0 is the equilibrium volume, and the C_{ij} are the elastic constants, with $i, j = 1...6 = xx, xy, zz, yz, zx, xy$. The elastic constants are determined by calculating E_{tot} as a function of $e_i e_j$ and taking the second energy derivative with respect to e_i and e_j. The hydrostatic pressure is obtained by calculating the change in volume of the supercell with respect to its equilibrium volume at ambient pressure V_0, which is related through the bulk modulus.

$$B = \frac{1}{3}\left(C_{11} - 2C_{12}\right). \tag{6}$$

After finding equilibrium lattice parameters of undeformed crystals by energy minimizations, shear deformation (γ) along the $[01\bar{1}0]$ direction has been applied to each simulation cell, as illustrated in Fig. 2.4. The atomic configurations have been then optimized so that all the forces acting on the atoms are below 0.005 eV/Å, and normal strains of each cell have been adjusted so that normal stress components are negligible. Shear stress τ has been determined for each value of the applied shear deformation using the compliability tensor.

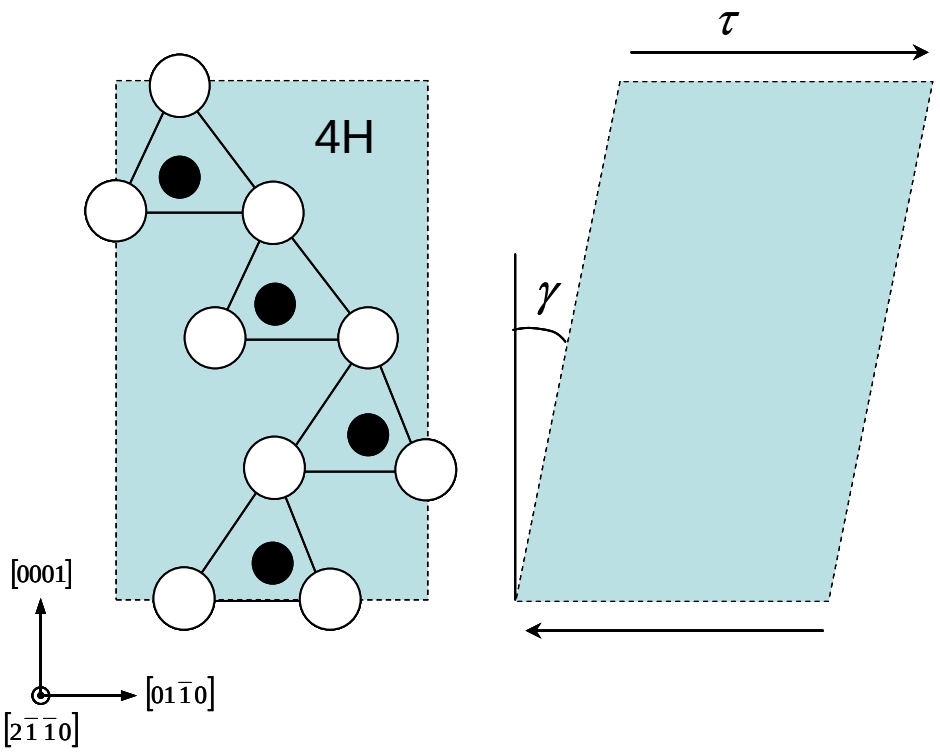

Fig. 2.4 Schematic of simulated shear deformation in hexagonal SiC: 4H polytype shown; γ = applied shear strain; τ = induced shear stress

For calculations at nonzero temperatures, the thermochemistry utilities of the Gaussian packages were used. From the total energy per atom (E_0), the Hemholtz free energy per site has been calculated as

$$F = E_0 + U_0 + F_{vib}(T), \tag{7}$$

where U_0 is the zero-point energy and F_{vib} is the temperature-dependent vibrational free energy, defined as

$$F_{vib}(T) = -k_B T \sum_{i,q} \log\left[2\sinh\left(\frac{h\nu_{iq}}{2k_B T} \right) \right]. \tag{8}$$

Here, k_B is Boltzmann constant, h is Planck constant, and ν_{iq} is the frequency of an optical phonon i with wavevector q, determined via density functional theory (DFT) linear response calculations[13] with q sampling at the distances between the K and Γ points of the Brillouin zone equal to 0, 1/3, 2/3, and 1.

To gain the insight on plastic deformation of SiC induced by SF dynamics at elevated pressures, we made assessment of the activation energies and slipping velocities of the stacking faults along the Shockley partials. The dislocation mobility is activated with energy Q as

$$\nu_{SP}(\theta, p) \propto \exp\left(\frac{Q - SFE(p)}{k_B T} \right), \tag{9}$$

where θ = 30° (90°) is the angle of a particular Shockley partial dislocation, k_B is Boltzmann constant, T is temperature, and p is pressure. Slipping along the stacking faults occurs only when the SF energy at a given pressure SFE(p) is greater than the activation energy Q. The calculations reveal that the activation energy Q is nearly independent of the type of SiC polytype or the pressure.[14] The results of activation energy calculation for a 634-atom Si-C-H cluster[14] and its normalization to a single atom are given in Panel A (Fig 2.5).

Dislocation core radii (Å)

30° Si-core	30° C-core	90° Si-core	90° C-core
$R_{30Si3C} := 5.3$	$R_{30C3C} := 4.5$	$R_{90Si3C} := 3.9$	$R_{90C3C} := 5.0$
$R_{30Si2H} := 5.5$	$R_{30C2H} := 4.7$	$R_{90Si2H} := 3.4$	$R_{90C2H} := 4.1$

Number of atoms in the cluster

$N_A := 210 + 210 + 214$ $\quad N_A = 634$

Activation energy for dislocation mobiliy (meV per cluster per unit length)

$Q_{30Si} := 4950$ $\quad Q_{90Si} := 4090$

$Q_{30C} := 4600$ $\quad Q_{90C} := 2740$

Activation energies for dislocation mobiliy (meV per atom)

$$Q_{30Si3C} := \frac{Q_{30Si}}{N_A} \cdot R_{30Si3C} \qquad Q_{30Si3C} = 41.4$$

$$Q_{30Si2H} := \frac{Q_{30Si}}{N_A} \cdot R_{30Si2H} \qquad Q_{30Si2H} = 42.9$$

$$Q_{30C3C} := \frac{Q_{30C}}{N_A} \cdot R_{30C3C} \qquad Q_{30C3C} = 32.6$$

$$Q_{30C2H} := \frac{Q_{30C}}{N_A} \cdot R_{30C2H} \qquad Q_{30C2H} = 34.1$$

$$Q_{90Si3C} := \frac{Q_{90Si}}{N_A} \cdot R_{90Si3C} \qquad Q_{90Si3C} = 25.2$$

$$Q_{90Si2H} := \frac{Q_{90Si}}{N_A} \cdot R_{90Si2H} \qquad Q_{90Si2H} = 21.9$$

$$Q_{90C3C} := \frac{Q_{90C}}{N_A} \cdot R_{90C3C} \qquad Q_{90C3C} = 21.6$$

$$Q_{90C2H} := \frac{Q_{30Si}}{N_A} \cdot R_{30Si3C} \qquad Q_{90C2H} = 41.4$$

Fig. 2.5 Panel A. Values of activation energy for slipping along the SF in SiC polytypes,[13] normalized to a single atom.

2.5 Results and Discussion

Single-point calculations of total energy were performed for varying lattice constants *a* and *c* near the expected equilibrium position. A total energy surface was then constructed, and the energy minimum corresponding to equilibrium lattice constants was determined by polynomial fitting. This is illustrated in Fig. 2.6 for the case of 3C SiC supercell. Once the optimum lattice constants were determined, the energy of the optimized supercell was calculated for each polytype. These total supercell energies, normalized to a single bond, were then used for calculation of spin interaction energies J_1, J_2, and J_3.

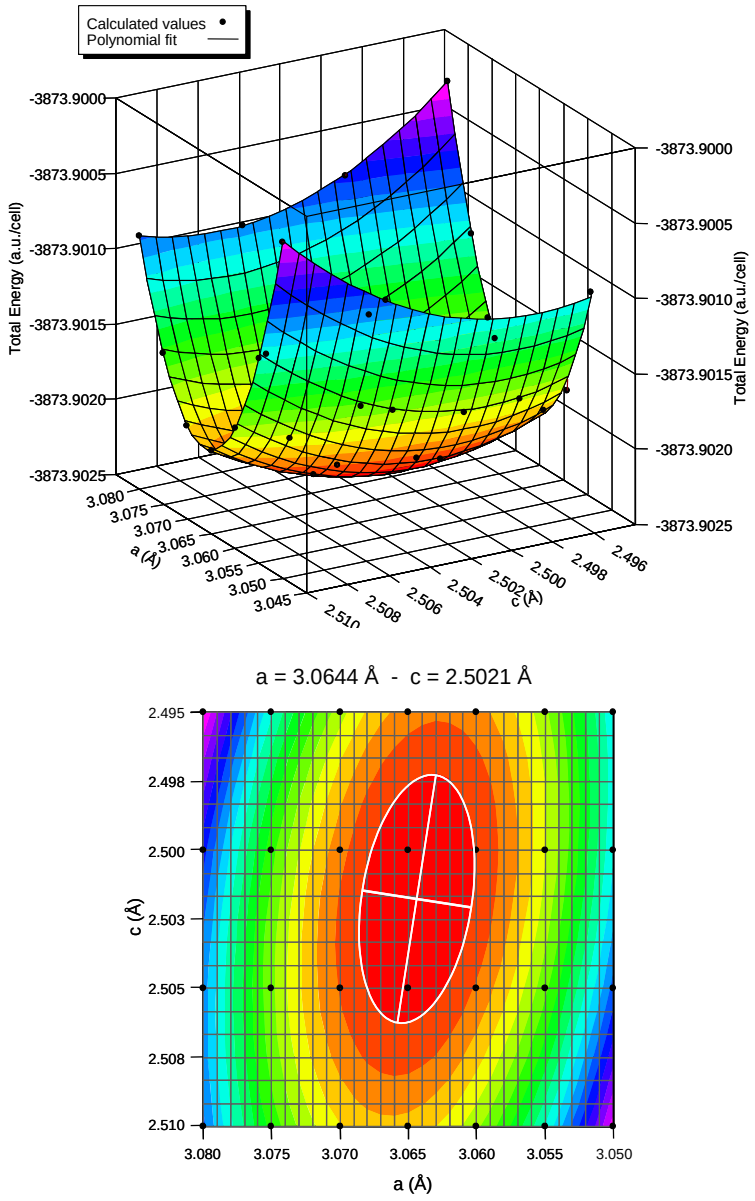

Fig. 2.6 Results of total energy minimization and the equilibrium lattice constants for 3C SiC superlattice

In a similar fashion, the optimized lattice parameters and the equilibrium supercell total energies were calculated for each polytype with a single B, N, O, or Al atom substituting for either Si or C in all available inequivalent *h* and *k* sites in a particular polytype. Taking cohesive energy as a criterion of lattice stability, it was observed that the B, N, and O atoms tend to substitute for C and that the Al atom tends to substitute for Si in the SiC lattice of all polytypes considered. This is in agreement with earlier experimental observations reported in literature.[15] Among all possible

substitutions for the C atom, the *k* site was found to be energetically more favorable in all cases. Therefore, only the lattices with B, N, and O in place of C and Al in place of Si in the *k* sites were considered in further calculations.

The addition of N, O, or Al to the SiC structure increased the lattice parameters and the dimensions of the supercell, to the largest extent in case of Al. Inversely, substituting C for B was leading to a decrease in the lattice parameters and the dimensions of the supercell. In general, the calculated lattice constants are in good agreement both with previous theoretical work and experimental observations.[4]

The spin interaction energies J_1, J_2, and J_3 calculated using Eq. 3 are listed in Table 2.2 Our results show reasonable correlation both with previously published data[3,5,16] and with the results of a similar work done at Rutgers for pure SiC polytypes.

The elastic constants for various SiC polytypes as a function of hydrostatic pressure were calculated following the procedure outlined in Eqs. 4–6. Only pure SiC structures (no additives) were considered for determination of elastic constants. Figure 2.7 summarizes the results of this calculation. There are only insignificant differences among the elastic constants of various hexagonal polytypes, therefore only the data for 2H SiC are presented.

Table 2.2 Spin interaction energies (meV/atom) for SiC with N, B, and O substituting for C and Al substituting for Si

Additive	J_1	J_2	J_3
SiC	1.64	–2.38	–0.15
SiC-B	1.57	–2.31	–0.07
SiC-N	1.74	–2.46	–0.23
SiC-O	1.79	–2.49	–0.29
SiC-Al	1.88	–2.61	–0.36

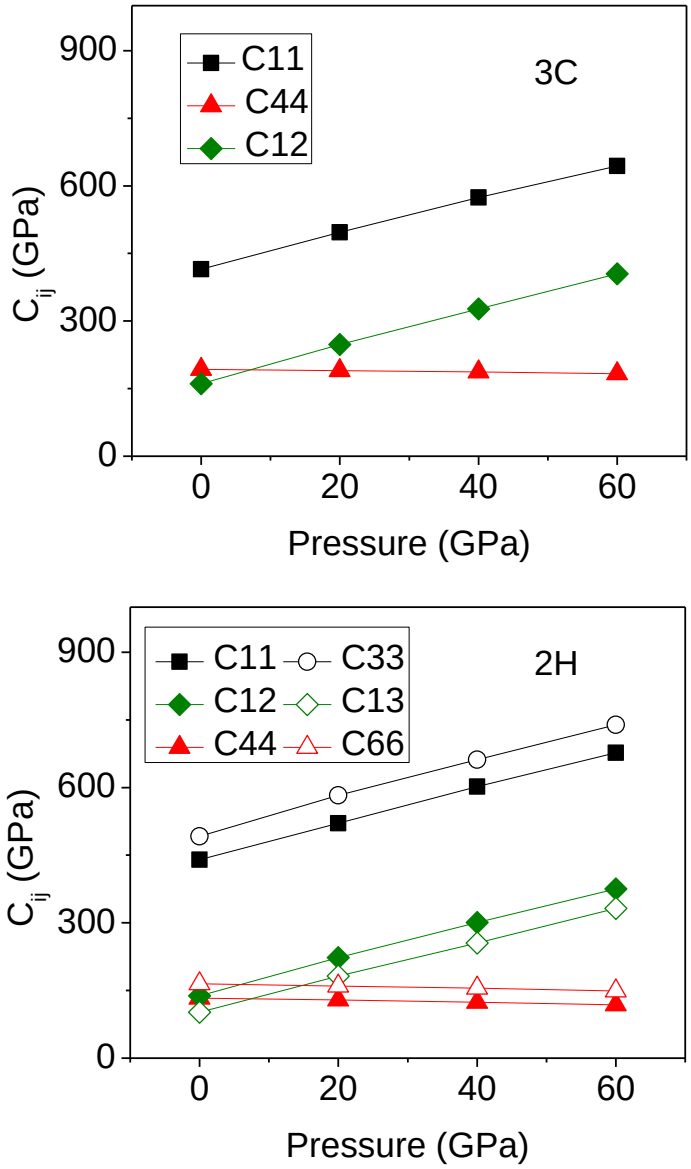

Fig. 2.7 Elastic constants as a function of hydrostatic pressure for cubic and hexagonal SiC polytypes

Figure 2.8 shows the calculated stress-strain curves for shear strain applied along the $[01\bar{1}0]$ direction on (0001) plane in 2H, 3C, 4H, and 6H SiC. Only pure SiC structures (no additives) were considered for this calculation. We observed that the stress-strain relations are nearly identical for all hexagonal polytypes up to $\gamma = 0.25$ and begin to deviate above this value.

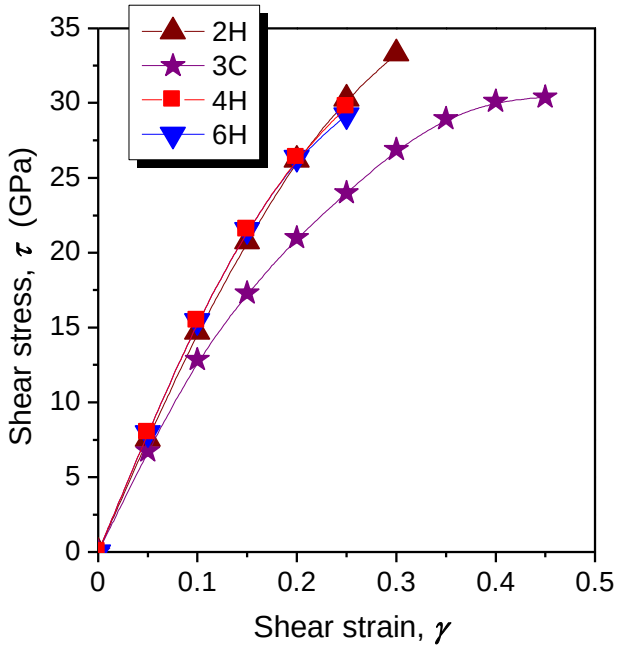

Fig. 2.8 Stress-strain curves in [$01\bar{1}0$] shear on (0001) plane of 2H, 3C, 4H, and 6H SiC polytypes

Knowledge of elastic constants allowed us to find lattice parameters of various SiC polytypes corresponding to each hydrostatic pressure value of 20 GPa, 40 GPa, and 60 GPa. Total energy calculations were performed at each lattice constants combination corresponding to a respective hydrostatic pressure value. Spin interaction energies were determined, and finally the stacking fault energies were calculated following Eq. 2. The results of this calculation are shown in Figs. 2.9–2.13. Adding B leads to a decrease in the SFE gradient with respect to hydrostatic pressure. Inversely, adding N, O, or Al is promoting an increase in the SFE pressure gradient for all SiC polytypes. Consequently, the SFE with positive gradient (3C, 4H, and both 6H SFs) are growing faster with hydrostatic pressure in the presence of N, O, or Al. In a similar way, the SFE with negative pressure gradients (2H) are falling faster with hydrostatic pressure in the presence of N, O, or Al. The situation is reverse for B as substitute in the SiC lattice.

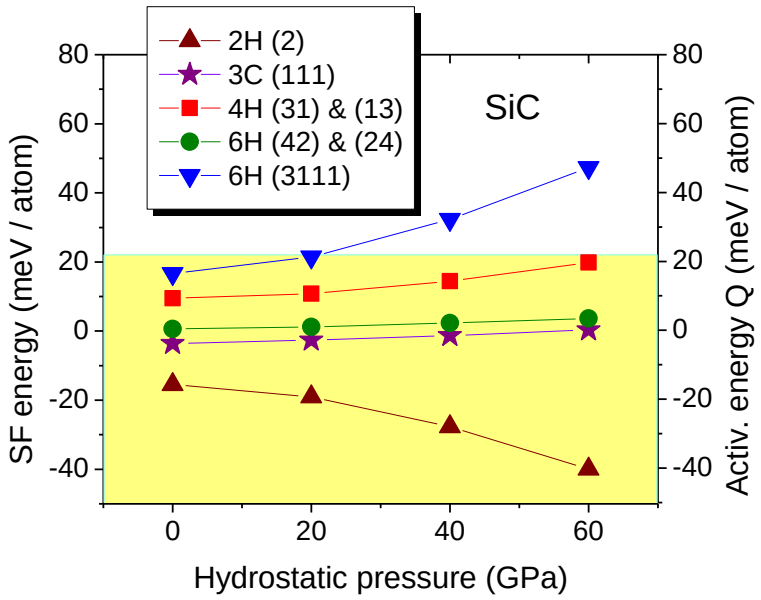

Fig. 2.9 SF energy as a function of hydrostatic pressure for SiC polytypes at the temperature of 0 K. The onset for plastic transformation is predicted at 20 GPa due to gliding of the (3111) SF in 6H SiC.

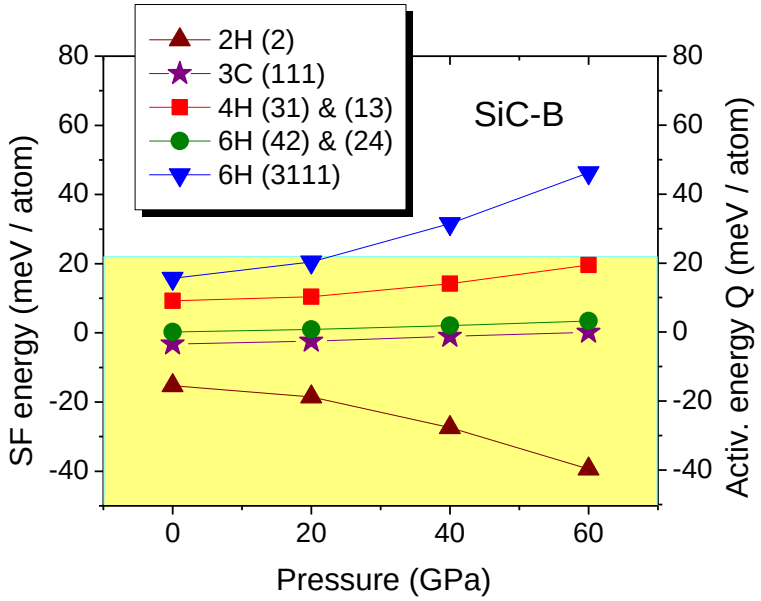

Fig. 2.10 SF energy as a function of hydrostatic pressure for SiC polytypes with B as an additive at the temperature of 0 K. The onset for plastic transformation is predicted at 22 GPa due to gliding of the (3111) SF in 6H SiC.

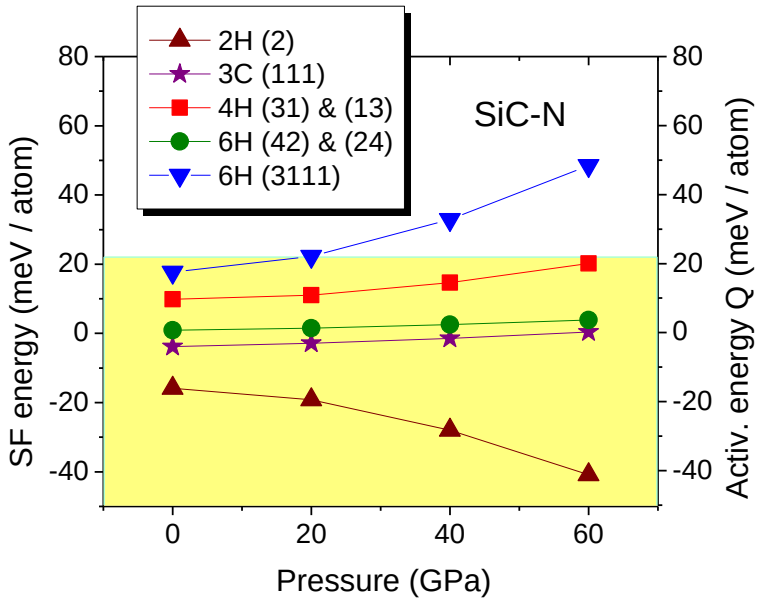

Fig. 2.11 SF energy as a function of hydrostatic pressure for SiC polytypes with N as an additive at the temperature of 0 K. The onset for plastic transformation is predicted at 19 GPa due to gliding of the (3111) SF in 6H SiC.

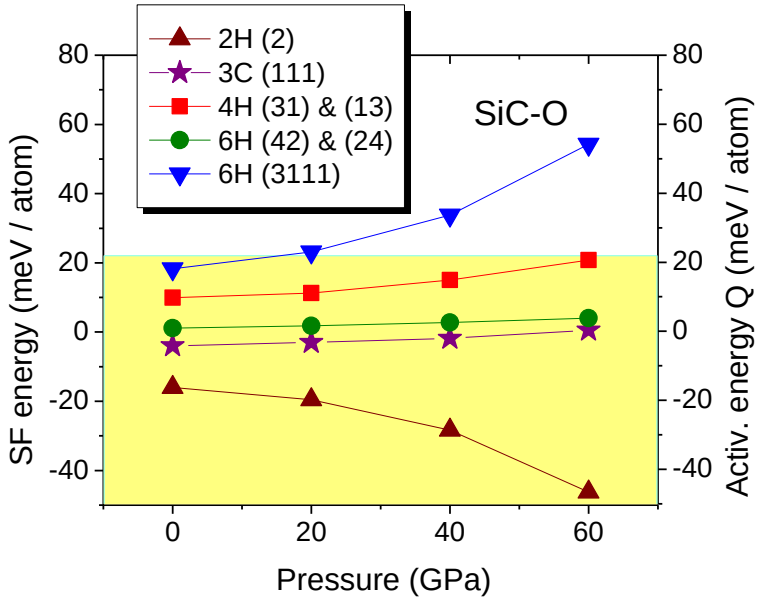

Fig. 2.12 SF energy as a function of hydrostatic pressure for SiC polytypes with O as an additive at the temperature of 0 K. The onset for plastic transformation is predicted at 16 GPa due to gliding of the (3111) SF in 6H SiC.

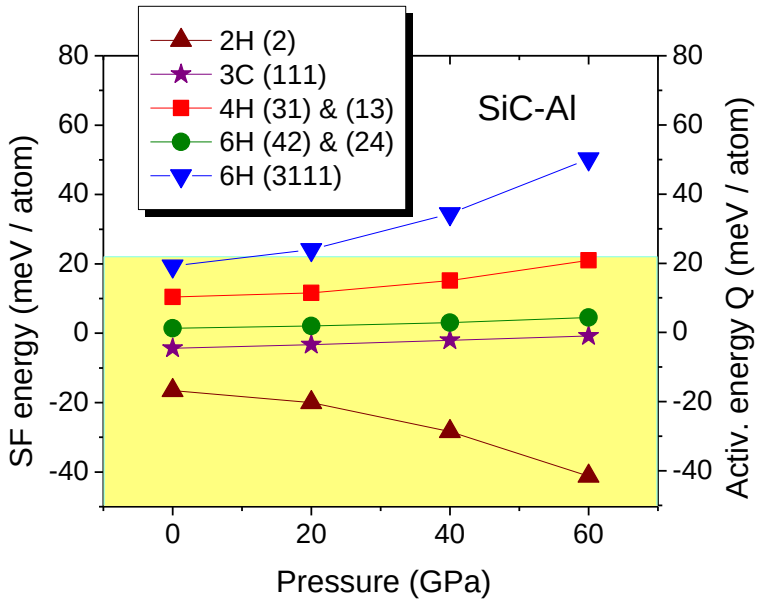

Fig. 2.13 SF energy as a function of hydrostatic pressure for SiC polytypes with Al as an additive at the temperature of 0 K. The onset for plastic transformation is predicted at 12 GPa due to gliding of the (3111) SF in 6H SiC.

In a similar fashion, total energy calculations and lattice optimizations were performed for each polytype for the values of shear stress corresponding to applied shear strains of $\gamma = 0.05$, 0.10, 0.15, 0.20, 0.25, and 0.30. Spin interaction energies were determined and finally the SF energies were calculated following Eq. 2. The results of this calculation are presented in Figs. 2.14–2.18. Again, similar to the hydrostatic pressure data, adding B leads to a decrease in the SF energy gradients with respect to shear stress, whereas the addition of N, O, or Al is increasing SF energy shear stress gradients for all SiC polytypes.

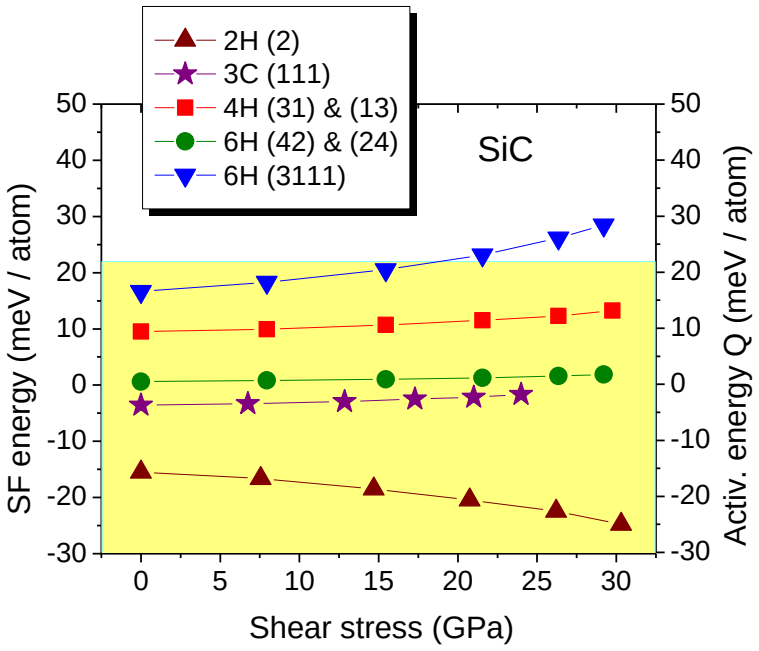

Fig. 2.14 SF energy as a function of shear stress for SiC polytypes at the temperature of 0 K. The onset for plastic transformation is predicted at 18.5 GPa due to gliding of the (3111) SF in 6H SiC.

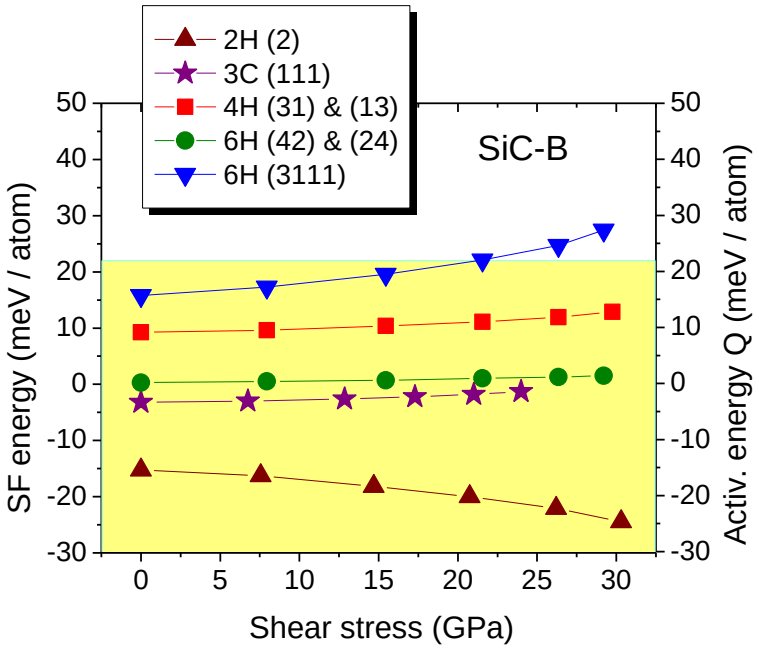

Fig. 2.15 SF energy as a function of shear stress for SiC polytypes with B as an additive at the temperature of 0 K. The onset for plastic transformation is predicted at 21.5 GPa due to gliding of the (3111) SF in 6H SiC.

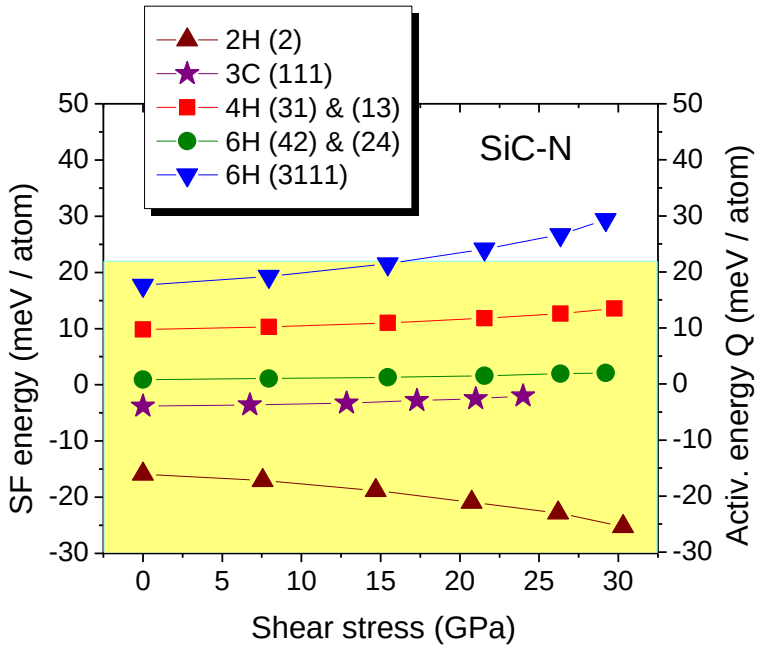

Fig. 2.16 SF energy as a function of shear stress for SiC polytypes with N as an additive at the temperature of 0 K. The onset for plastic transformation is predicted at 16.5 GPa due to gliding of the (3111) SF in 6H SiC.

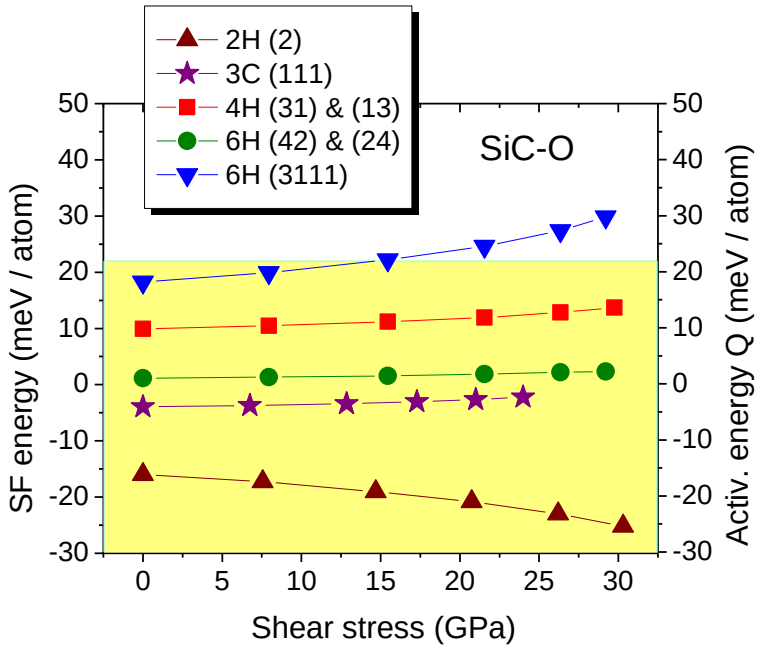

Fig. 2.17 SF energy as a function of shear stress for SiC polytypes with O as an additive at the temperature of 0 K. The onset for plastic transformation is predicted at 15 GPa due to gliding of the (3111) SF in 6H SiC.

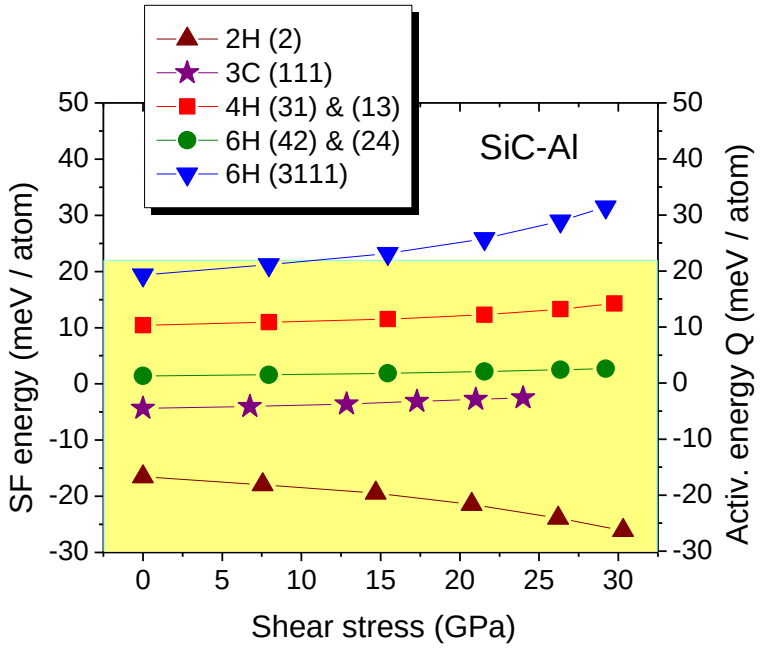

Fig. 2.18 SF energy as a function of shear stress for SiC polytypes with Al as an additive at the temperature of 0 K. The onset for plastic transformation is predicted at 11 GPa due to gliding of the (3111) SF in 6H SiC.

The SF energy as a function of hydrostatic pressure or shear stress was estimated against the activation energy *Q* for gliding in the SiC basal plane. The data for *Q* were taken from Panel A for the case of 90° Si-core partial dislocation (21.9 meV/atom) as the one that requires minimum activation energy. As can be seen in Figs. 2.9–2.18, adding N, O, or Al (in the concentrations considered here, specifically 1/24) decreases the onset for plastic deformation through gliding of the (3111) SFs in 6H SiC polytype, while adding B increases this critical pressure. The predicted SF-induced plasticity onsets in SiC under hydrostatic pressure and shear stress are shown in Fig. 2.19. As follows from analysis of Fig. 2.19, Al in particular significantly reduced SF-induced plasticity onset. In all cases, SF-induced plasticity in SiC is predicted to start at lower stresses under shear deformation as compared with purely hydrostatic compression.

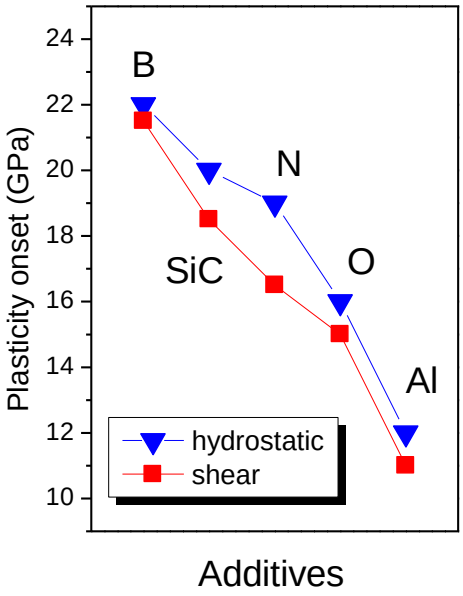

Fig. 2.19 Plasticity onset due to SF mobility in pure SiC and in SiC with B, N, O, and Al as substitutional additives under hydrostatic and iniaxial compression

To estimate the effect of temperature on SF mobility in SiC, the approach outlined in Eqs. 7 and 8 was used. Only room temperature (300 K) was considered in this reporting period. The results of room-temperature calculations for pure SiC and SiC doped with B, N, O, and Al under hydrostatic compression are shown in Figs. 2.20–2.24 and under shear deformation in Figs. 2.25–2.29. Increase in temperature brings the SF energy curves closer together in all cases. This effectively moves farther along the pressure axis the point where the (3111) 6H SF energy curve crosses the line describing the activation energy for gliding in the SiC basal plane. A comparison of the predicted SF-induced plasticity onsets in SiC under hydrostatic pressure and shear stress at zero and room temperatures is shown in Fig. 2.30.

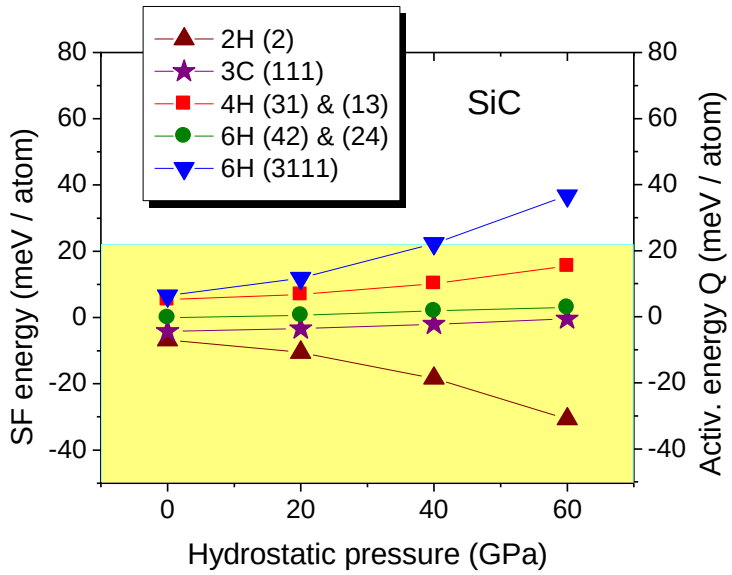

Fig. 2.20 SF energy as a function of hydrostatic pressure for SiC polytypes at 300 K. The onset for plastic transformation is predicted at 40 GPa due to gliding of the (3111) SF in 6H SiC.

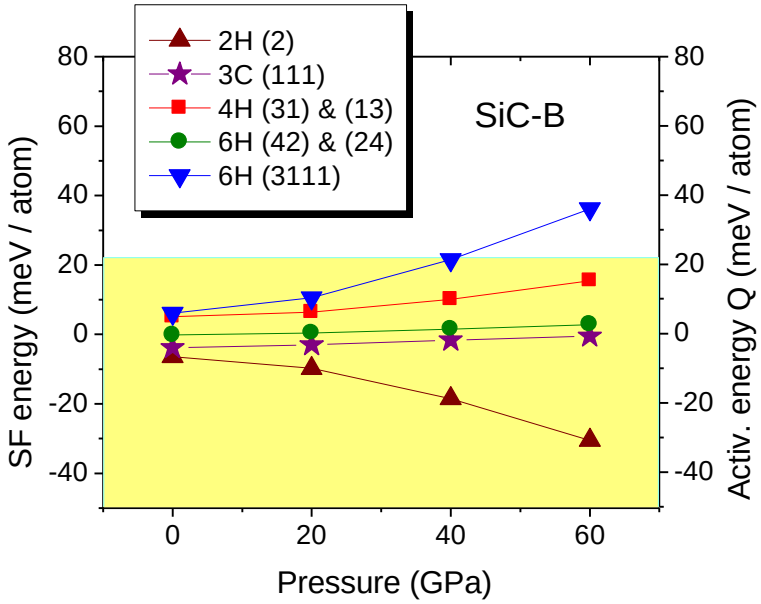

Fig. 2.21 SF energy as a function of hydrostatic pressure for SiC polytypes with B as an additive at 300 K. The onset for plastic transformation is predicted at 40.5 GPa due to gliding of the (3111) SF in 6H SiC.

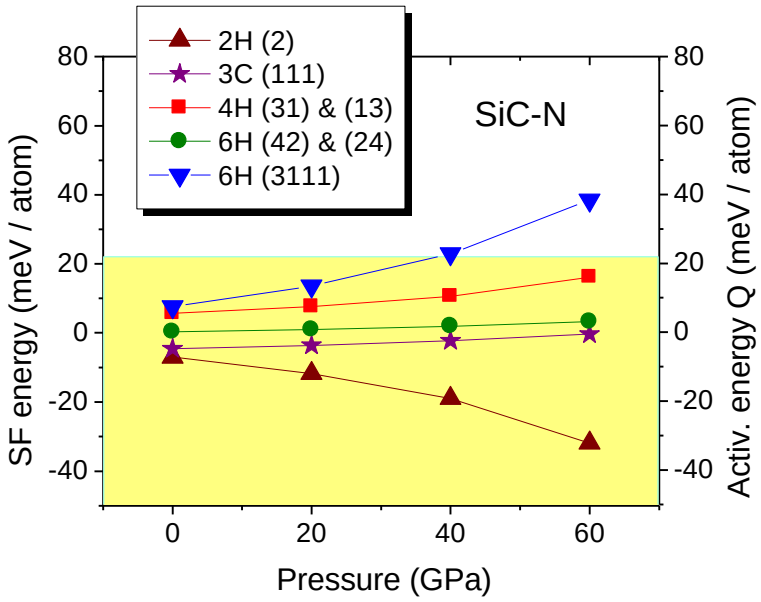

Fig. 2.22 SF energy as a function of hydrostatic pressure for SiC polytypes with N as an additive at 300 K. The onset for plastic transformation is predicted at 38 GPa due to gliding of the (3111) SF in 6H SiC.

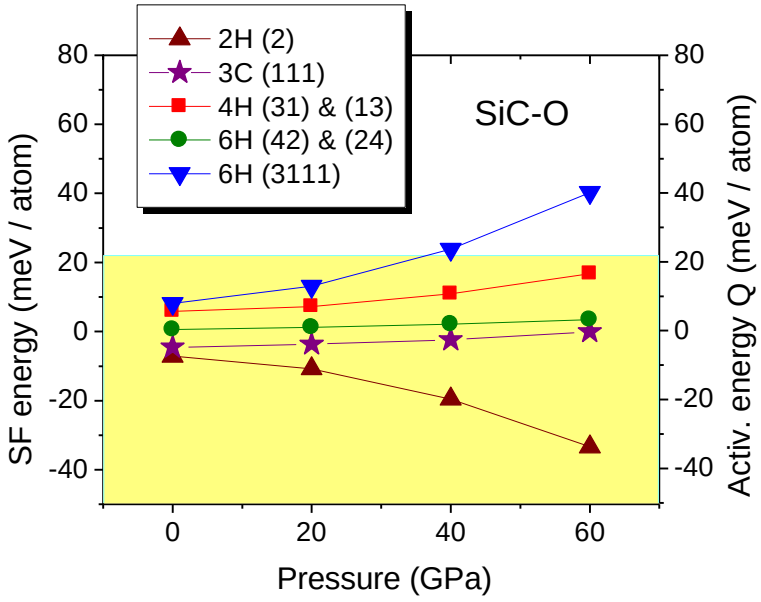

Fig. 2.23 SF energy as a function of hydrostatic pressure for SiC polytypes with O as an additive at 300 K. The onset for plastic transformation is predicted at 37.5 GPa due to gliding of the (3111) SF in 6H SiC.

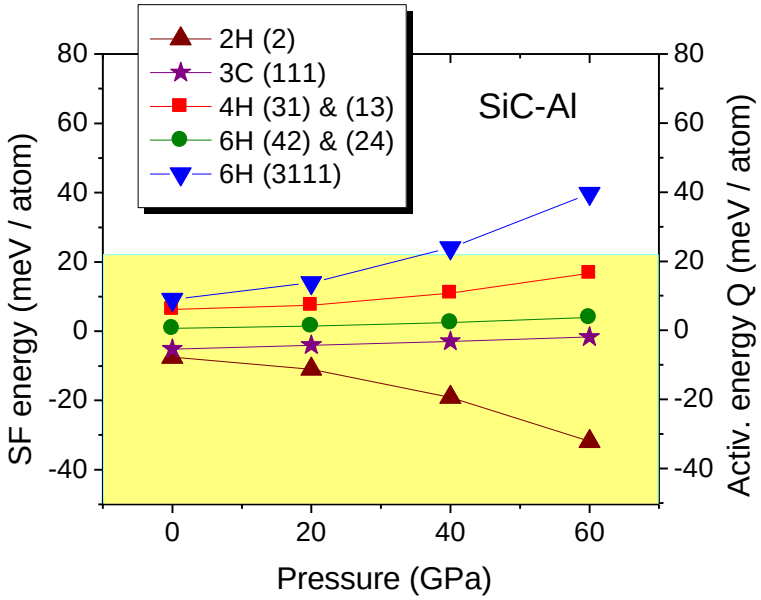

Fig. 2.24 SF energy as a function of hydrostatic pressure for SiC polytypes with Al as an additive at 300 K. The onset for plastic transformation is predicted at 36 GPa due to gliding of the (3111) SF in 6H SiC.

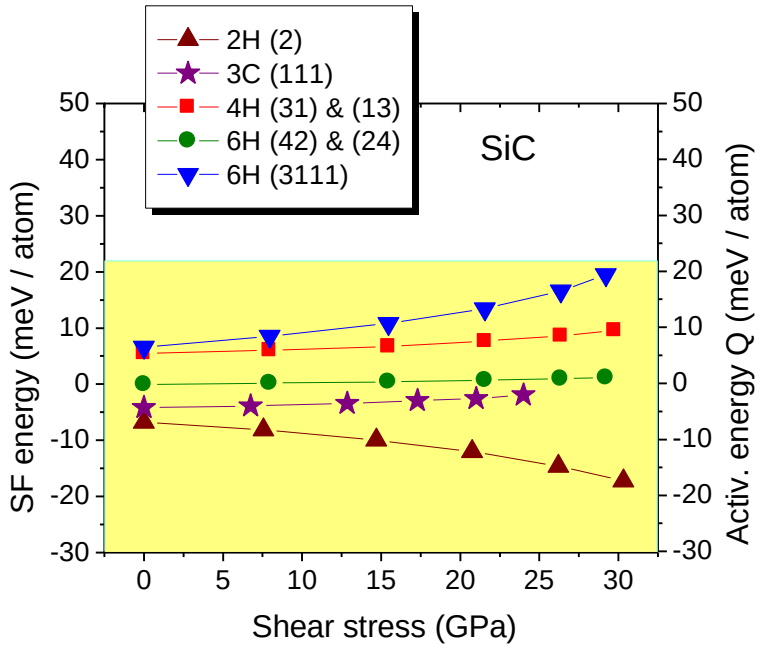

Fig. 2.25 SF energy as a function of shear stress for SiC polytypes at 300 K. The onset for plastic transformation is predicted at 31 GPa due to gliding of the (3111) SF in 6H SiC.

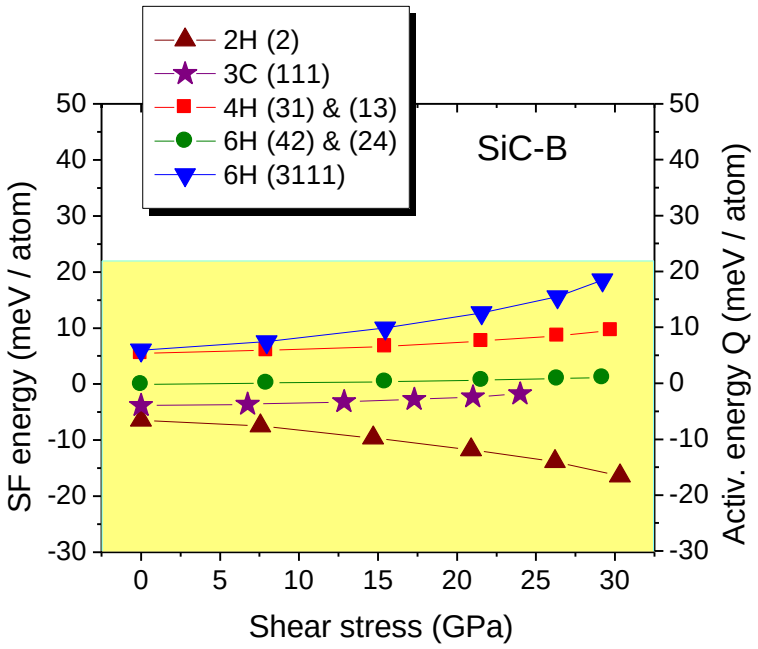

Fig. 2.26 SF energy as a function of shear stress for SiC polytypes with B as an additive at 300 K. The onset for plastic transformation is predicted at 32 GPa due to gliding of the (3111) SF in 6H SiC.

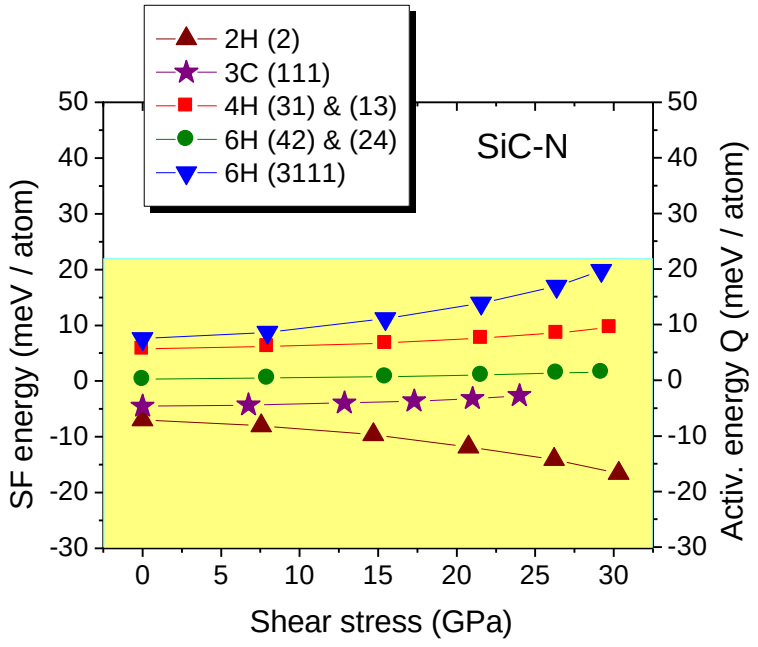

Fig. 2.27 SF energy as a function of shear stress for SiC polytypes with N as an additive at 300 K. The onset for plastic transformation is predicted at 30.5 GPa due to gliding of the (3111) SF in 6H SiC.

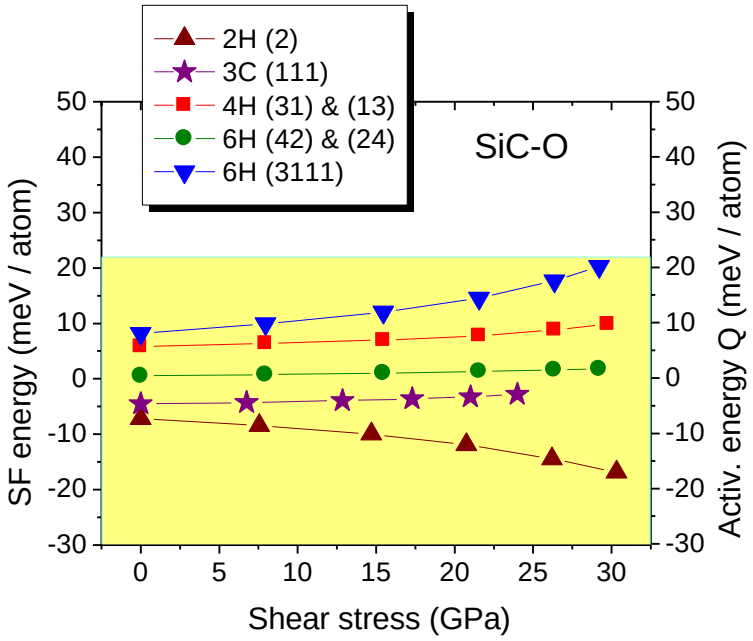

Fig. 2.28 SF energy as a function of shear stress for SiC polytypes with O as an additive at 300 K. The onset for plastic transformation is predicted at 30 GPa due to gliding of the (3111) SF in 6H SiC

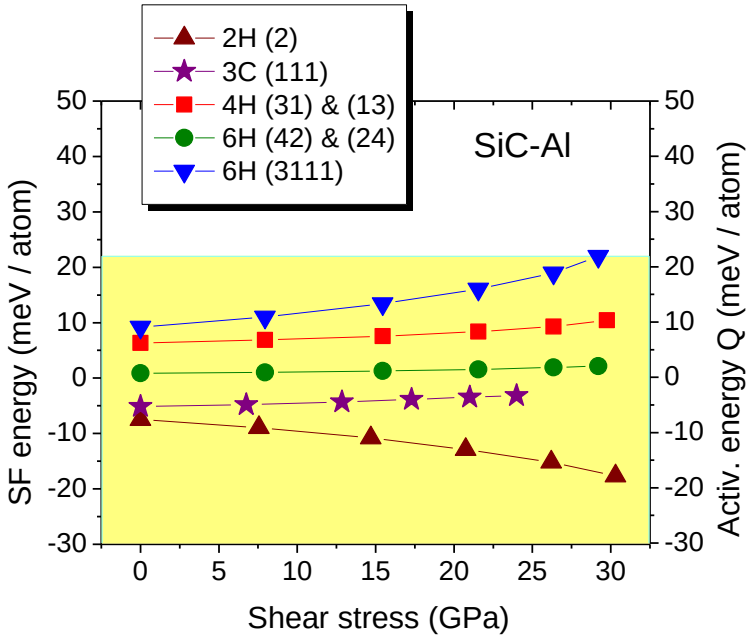

Fig. 2.29 SF energy as a function of shear stress for SiC polytypes with Al as an additive at 300 K. The onset for plastic transformation is predicted at 29 GPa due to gliding of the (3111) SF in 6H SiC

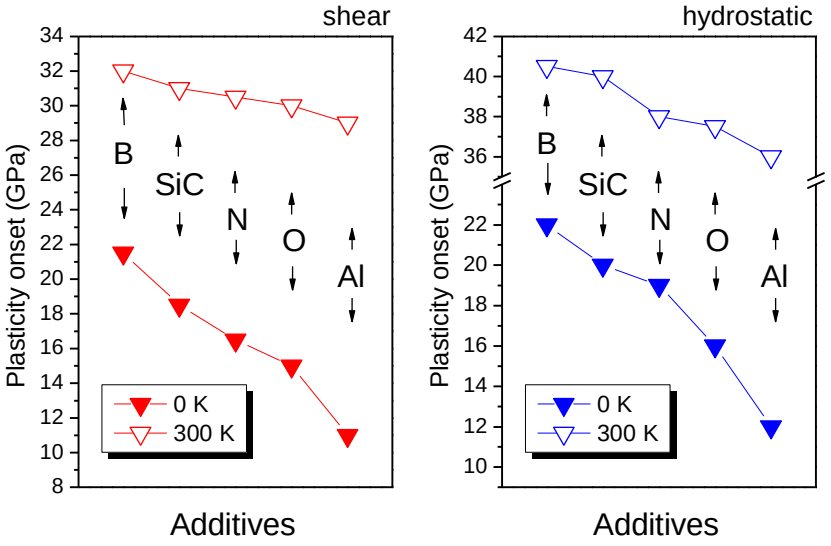

Fig. 2.30 The effect of temperature on plasticity onset due to SF mobility in pure SiC and in SiC with B, N, O, and Al as substitutional additives under shear stress (left) and hydrostatic compression (right).

2.6 Future Work

Future work will address the role of intrinsic stress/external confinement and the influence of nonrigid grain boundaries on SF dynamics in SiC. We also plan to investigate the influence of interfaces between different polytypes on SiC plasticity in a range of pressures.

SF energies will be directly calculated using larger supercells consisting of 96 atoms. The choice of such large supercells is justified by the requirement that the SFs in the neighboring supercells should not interact. The symmetry of the resulting supercells will be rhombohedral to preserve periodicity of the crystal lattice.

2.7 References

1. Dandekar DP. Aberdeen Proving Ground (MD): Army Research Laboratory (US); 2002. Report No.: ARL-TR-2695.
2. Hong MH, Samant AV, Pirouz P. Philos Mag A. 2000;80:919.
3. Käckell P, Furthmüller J, Bechstedt. F Phys Rev. 1998;B58:1326.
4. Lindefelt U, Iwata H, Öberg S, Briddon PR. Phys Rev B. 2003;67:155204
5. Cheng C, Needs RJ, Heine V. J Phys. 1988;C21:1049.
6. Hohenberg P, Kohn W. Phys Rev. 1964;136:B864.
7. Kohn W, Sham L. Phys Rev. 1965;140:A1133.
8. Slater JC. Quantum theory of molecular and solids, Vol. 4: The self-consistent field for molecular and solids; New York: McGraw-Hill; 1974.
9. Vosco SH, Wilk L, Nusair M. Can J Phys. 1980;58:1200.
10. Hehre WJ, Stewart RF, Pople JA. J Chem Phys. 1969;51:2657.
11. Collins JB, Schleyer PvR, Binkley JS, Pople JA. J Chem Phys. 1974;64: 5142.
12. Mayer B, Anton H, Bott E. et al. Intermetallics 2003;11:23.
13. Baroni S, Gironcoli S, Corso AD et al. Rev Mod Phys. 2001;73:515.
14. Blumenau AT, Fall CJ, Jones R. et al. Phys Rev. 2003;B 68:174108.
15. Ikeda M, Matsunami H, Tanaka T. Phys Rev. 1980;B 22;2842.
16. Karch K, Wllenhofer G, Pavone P. et al. In: Lockwood D, editor. Proceedings of the 22nd International Conference on the Physics of Semiconductors; 1994; Vancouver. Singapore: World Scientific; 1995; p. 401.

3. Part 2, Task 9: Study of United States Silicon Carbide (SiC) Powder Variations (2011)

Core Faculty: RA Haber, DE Niesz

US Army Research Laboratory (ARL) Collaborator: T Jessen

Research Associate: V Domnich

Undergraduate Student: M Freeman

3.1 Long-Range Goals

- Develop a better understanding of the reaction during carbothermic production of silicon carbide (SiC).
- Quantify the effects of precursor impurities, reaction time, and spatial location on chemistry and crystallinity of SiC for dynamic energy dissipation applications.

3.2 Background

It is difficult, if not impossible, to fabricate high-quality ceramic components without control of the powders comprising them. US-based companies supplying many strategic ceramic components have seen the erosion of domestic suppliers over the past 2 decades. Many critical material-based systems for high-strain-rate mechanical or thermal-loading applications rely on unique, highly specified powders. Applications ranging from personnel or vehicular armor to high-intensity mirrors to missile radomes to rocket nozzles are fabricated using powders coming less from the United States and more from countries such as India, China, and Russia. The consequence of this eroded domestic supply base has been the inability of component manufacturers to design powders for a specific application, instead sorting or treating highly variable commodity powders to impart the requisite material "uniqueness" for an application.

For commercial-scale operations, SiC powders are produced by the carbothermic reduction of a silicon oxide (SiO) in contact with a carbon (C) source. This is known as Acheson process.[1] The resultant powder is coarse in grain size and must be comminuted to produce micron to submicron-sized particles required for ceramic processing. In many cases, lower cost, lower specified end-use applications, such as abrasives, have introduced new developing world powder suppliers. With greater dependence on foreign sources, supplied quality has become variable. Furnace

reactors were once large-scale operations; now small producers can introduce very small, highly variable product into a distribution stream. As an example, one supplier can produce 500 lb while a second producer can produce 5–10 tons. Precursor raw materials are also in question. Traditional C sourcing used to be high-grade-petroleum-derived coke; however, in China it is not uncommon to see anthracite coal used. The consequence is a highly chemically variable end product. For carbide powders, the impact of trace impurity variations is to provide variable levels of crystallinity into the supply stream. Component suppliers are now faced with how to make a consistent product that meets today's military specifications. The concepts related to improving component performance for the future can no longer include changing the initial powder: It is no longer in our control.

By losing control of powder processing, the United States has reached a point where variability in carbide powders are expected, tolerated, and in many cases ignored. Process treatments are developed to "treat" variable powders to improve their overall uniformity. However, this results in dense components whose microscale variability reflects the intrinsic variability of the parent powder. From a simple business or logistic point of view, manufacturers can no longer assure that the carbide powders used in highly specified components would meet strict testing requirements.

In this research program, we will specifically investigate how new phenomenological performance enhancements can be achieved by manipulating the intrinsic properties of powders used in processing. Keeping in mind that the goal of this research will be to manage future strategic defense materials, we will examine how SiC powders can be manipulated during their synthesis, thereby providing a bases for creating or improving the limited domestic supply chain. We will also examine the limitations an uncontrollable imported powder supply has on the prospects for improved materials in the future.

3.3 Experimental Approach

A piece of SiC produced by carbothermic reaction was acquired from Washington Mills (Niagara Falls, NY). To investigate variations in chemical composition and properties of SiC as a function of distance from electrode, samples were retrieved at each 2 inches from the electrode edge to the metallurgical grade edge, as illustrated in Fig. 3.1. As the first step in powder reduction, a Fritsch Pulverisette jaw crusher was used to reduce the samples to particles of sizes in the range of 1–10 mm. Final jet milling of powders to submicron sizes was achieved in a Sturgevant Qualification Micronizer. Particle size analysis was performed using a Mastersizer unit by Malvern Instruments. Samples were densified using a Thermal

Technology spark plasma sintering (SPS) unit at the maximum temperature of 1,950 °C. To achieve maximum density of the samples, about 1% of boron carbide (B_4C) and excess C as graphite (B/C mole ratio of 0.72) were mixed with SiC powders prior to sintering. These samples are referred to as samples with sintering aids. Once the jet milling and sintering parameters to produce ceramics with near theoretical density were established, new batches of powders were sintered without the use of the sintering aids.

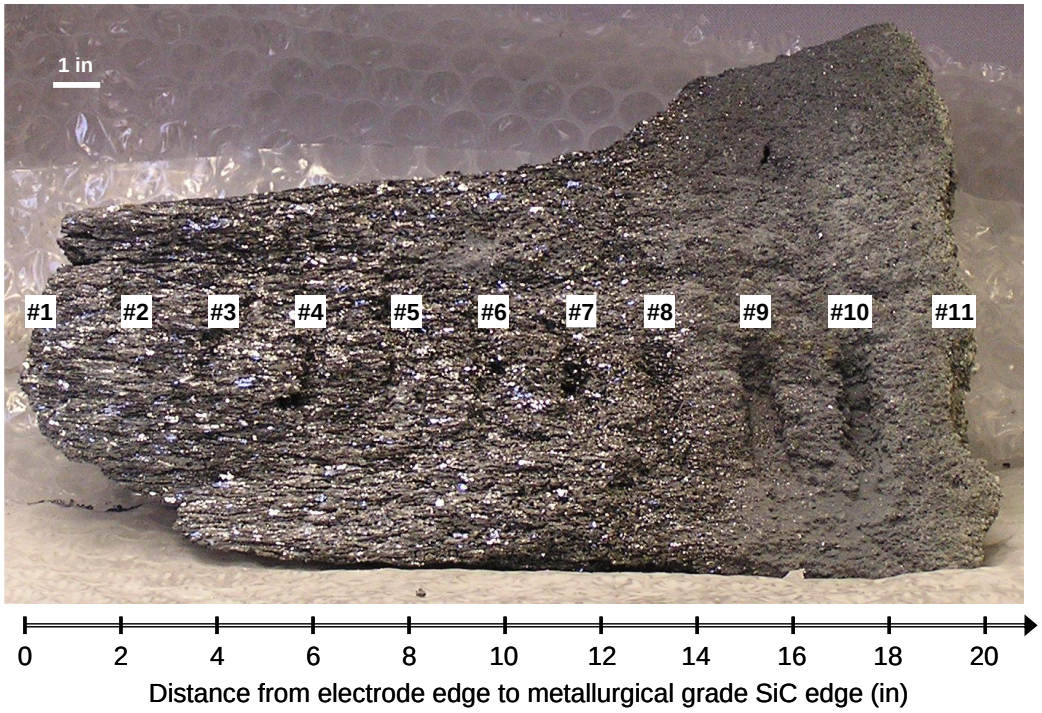

Fig. 3.1 SiC piece retrieved from a carbothermic reactor. The samples for analysis were collected from different zones as indicated by consecutive numbers in the direction of increasing distance from the electron edge toward the metallurgical-grade SiC edge.

The density of sintered samples was determined using the Archimedes method. Elastic properties (elastic modulus, bulk modulus, shear modulus) of the sintered samples were determined using a high-frequency ultrasound system, developed at Rutgers University, capable of pulse amplitude and time-of-flight C-scan imaging and acoustic spectroscopy via fast Fouier transform analysis of sample peak response. Hardness measurements were performed on a Leco hardness tester using a Knoop indenter at 1-kg load. Hardness data were averaged over 30 measurements on each sample.

Raman spectroscopy analysis was performed using a Renishaw InVia unit equipped with a 633-nm wavelength laser and a 1,200/mm diffraction grating. A 20× objective lens was used, which allowed focusing the laser beam to a 4-μm spot on the sample surface. Spectra were acquired both at maximum and reduced laser power to verify that no artifacts were introduced by overheating of materials within the laser illuminated area. On each sample, spectra were acquired from 10 randomly selected areas to obtain statistically significant results.

Raman analysis of SiC polytypes was based on the methodology developed by Patrick et al.[2–5] because different SiC polytypes have different numbers of atoms per unit cell and they have different numbers of phonon branches in the Brillouin zone (BZ). For a periodic crystal, Raman measurements can access only the phonons with vectors $q = 0$ in the BZ scheme. In the large zone (LZ) representation, which unfolds the BZ phonon dispersion curves in the axial direction up to q_{max}, the phonon dispersion curves become nearly independent of polytype (Fig. 3.2). Points of this common LZ spectrum accessible to Raman measurements have special values of the reduced momentum $X = q / q_{max}$ that are equivalent to $q = 0$ in the BZ representation. These special points on the phonon dispersion curves in the large zone are characterized by small energy discontinuities for all accessible reduced momentum values, except for X = 0.

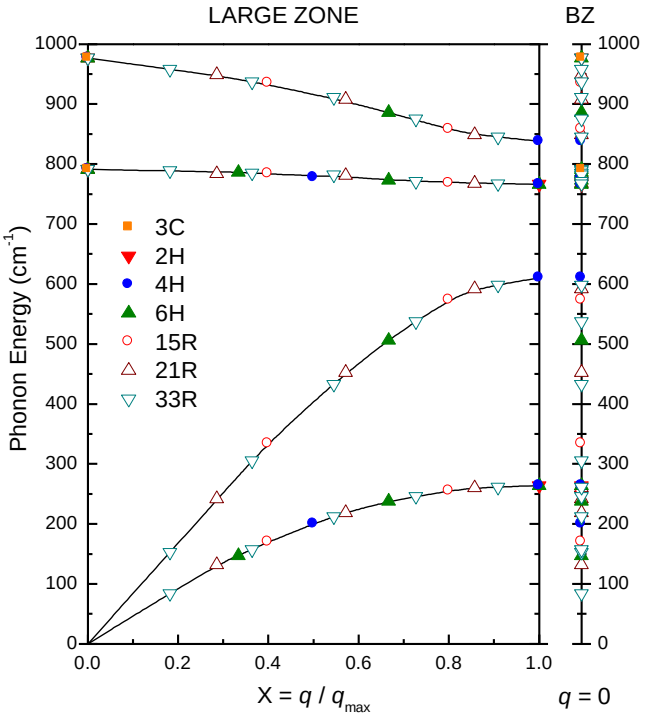

Fig. 3.2 LZ representation of phonon dispersion spectra in various SiC polytypes. The position of the special points on the reduced momentum axis and the Raman active modes for each polytype are related to the number of atoms in the unit cell of a respective polytype. Also shown are equivalent Raman modes at $q = 0$ in the BZ.

The use of the LZ scheme allows identification of different SiC polytypes by Raman spectroscopy measurement. In particular, the bands at 200 cm^{-1}, 610 cm^{-1}, and 837 cm^{-1} are unique to the 4H polytype; the bands at 147 cm^{-1}, 238 cm^{-1}, 506 cm^{-1}, and 886 cm^{-1} are unique to the 6H polytype; the bands at 170 cm^{-1}, 255 cm^{-1}, 334 cm^{-1}, 573 cm^{-1}, and 858 cm^{-1} are unique to the 15R polytype, the bands at 132 cm^{-1}, 219 cm^{-1}, 453 cm^{-1}, 592 cm^{-1}, and 908 cm^{-1} are unique to the 21R polytype; and the bands at 84 cm^{-1}, 305 cm^{-1}, 433 cm^{-1}, 537 cm^{-1}, 598 cm^{-1}, 875 cm^{-1}, and 958 cm^{-1} are unique to the 33R polytype (Fig. 3.3). At the same time, the bands in the range of 238–264 cm^{-1}, 766–791 cm^{-1}, and the bands at 977 cm^{-1} may belong to any of 3C, 2H, 4H, 6H, 15R, 21R, or 33R polytypes and therefore only allow identification of SiC without providing exact information on its polytype structure.

In addition to various SiC polytypes, free Si (a single narrow band at 520 cm^{-1} [6]) and graphitic C (D and G bands[7]) were identified in selected samples by Raman spectroscopy (Fig. 3.3).

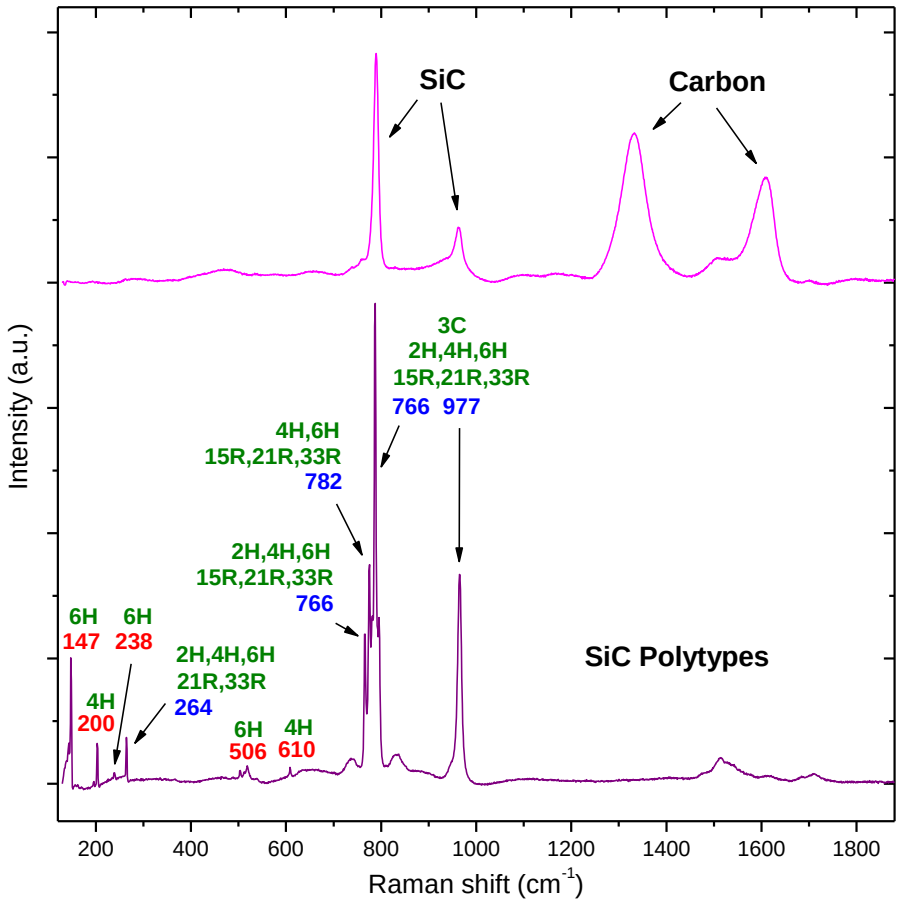

Fig. 3.3 Typical Raman spectrum of SiC showing bands specific to a particular SiC polytype (red) and overlapping bands of several SiC polytypes (blue). Only 2 bands at 766 and 977 cm^{-1} should be observed in 3C SiC.

3.4 Results and Discussion

The results of our Raman analysis of the samples obtained from various zones in the carbothermally reduced SiC piece corresponding to different steps of powder reduction and sintering are summarized in Tables 3.1–3.5 According to Raman data, 6H polytype is the major component in areas 1–4 (Fig. 3.4). Further, as shown in Fig. 3.5, the 4H SiC polytype often becomes a predominant component in areas 6–9 (midzone between the SiC edge adjacent to graphitic electrode and the furthest from the electrode metallurgical-grade SiC edge). The 15R SiC polytype and free Si are also sometimes observed in areas 6–9. In areas 10 and 11, identifying the polytype structure of SiC becomes problematic, although the presence of SiC can be confirmed in most cases. Closer to the metallurgical-grade edge (areas 8–11), free C becomes a predominant component in the sample chemistry (Fig. 3.6). We also note the presence of the 33R SiC polytype as a minor contribution in some analyzed samples. The results of our Raman analysis for 6H SiC, 4H SiC, 15R SiC, and free C are displayed in Fig. 3.7. As evident from Fig. 3.7, powder processing and sintering with the use of sintering aids do not change qualitatively the distribution of the main chemical components; the quantitative change is in the increased amount of 4H and 15R SiC in the midzone as the powders are reduced to micron size.

Table 3.1 Summary of the results of Raman analysis of unprocessed SiC

Sample No.	Distance from Electrode Edge (inches)	SiC Polytypes Identified (% of all observations)						Graphitic C Detected	Free Si Detected
		3C	2H	4H	6H	15R	33R		
1	0	+ –	+ –	0	100	0	30	0	0
2	2	+ –	+ –	0	100	0	40	0	0
3	4	+ –	+ –	0	100	0	30	0	0
4	6	+ –	+ –	0	100	0	30	0	0
5	8	+ –	+ –	10	80	0	30	0	0
6	10	+ –	+ –	70	20	20	20	0	10
7	12	+ –	+ –	40	30	10	30	0	10
8	14	+ –	+ –	70	20	10	10	10	0
9	16	+ –	+ –	30	70	10	20	70	0
10	18	+ –	+ –	10	10	0	30	70	0
11	20	+ –	+ –	10	10	0	10	100	0

Table 3.2 Summary of the results of Raman analysis of crushed SiC powders

Sample No.	Distance from Electrode Edge (inches)	SiC Polytypes Identified (% of all observations)						Graphitic C Detected	Free Si Detected
		3C	2H	4H	6H	15R	33R		
1	0	+ –	+ –	0	100	0	10	0	0
2	2	+ –	+ –	0	100	0	10	0	0
3	4	+ –	+ –	0	100	0	10	0	10
4	6	+ –	+ –	20	80	10	10	0	20
5	8	+ –	+ –	30	70	10	10	0	10
6	10	+ –	+ –	40	70	20	30	0	0
7	12	+ –	+ –	70	30	10	10	0	0
8	14	+ –	+ –	10	80	20	30	40	0
9	16	+ –	+ –	30	70	0	50	70	0
10	18	+ –	+ –	20	40	0	60	60	0
11	20	+ –	+ –	10	30	0	50	100	20

Table 3.3 Summary of the results of Raman analysis of milled SiC powders

Sample No.	Distance from Electrode Edge (inches)	SiC Polytypes Identified (% of all observations)						Graphitic C Detected	Free Si Detected
		3C	2H	4H	6H	15R	33R		
1	0	+ –	+ –	10	100	0	0	0	0
2	2	+ –	+ –	0	100	10	0	0	0
3	4	+ –	+ –	0	100	0	10	0	0
4	6	+ –	+ –	40	100	20	0	0	0
5	8	+ –	+ –	100	100	60	0	0	0
6	10	+ –	+ –	100	90	50	10	0	0
7	12	+ –	+ –	100	70	30	0	0	0
8	14	+ –	+ –	90	100	10	0	30	0
9	16	+ –	+ –	80	100	30	0	40	0
10	18	+ –	+ –	10	80	10	0	90	0
11	20	+ –	+ –	20	60	0	0	100	0

Table 3.4 Summary of the results of Raman analysis of sintered SiC ceramics (with sintering aids)

Sample No.	Distance from Electrode Edge (inches)	SiC Polytypes Identified (% of all observations)						Graphitic C Detected	Free Si Detected
		3C	2H	4H	6H	15R	33R		
1	0	+ –	+ –	0	100	0	0	0	0
2	2	+ –	+ –	0	100	0	0	0	0
3	4	+ –	+ –	0	100	0	0	0	0
4	6	+ –	+ –	80	100	20	0	0	0
5	8	+ –	+ –	90	100	30	0	0	0
6	10	+ –	+ –	90	50	20	0	0	0
7	12	+ –	+ –	100	30	0	0	0	0
8	14	+ –	+ –	80	60	20	0	70	0
9	16	+ –	+ –	100	50	20	0	50	0
10	18	+ –	+ –	50	90	30	0	100	0
11	20	+ –	+ –	80	90	30	0	100	0

Table 3.5 Summary of the results of Raman analysis of sintered SiC ceramics (no sintering aids)

Sample No.	Distance from Electrode Edge (inches)	SiC Polytypes Identified (% of all observations)						Graphitic C Detected	Free Si Detected
		3C	2H	4H	6H	15R	33R		
1	0	NA	NA	NA	NA	NA	NA	NA	NA
2	2	+ –	+ –	0	100	0	0	0	0
3	4	NA	NA	NA	NA	NA	NA	NA	NA
4	6	+ –	+ –	90	100	0	0	0	0
5	8	NA	NA	NA	NA	NA	NA	NA	NA
6	10	+ –	+ –	90	60	10	0	0	0
7	12	+ –	+ –	100	40	0	0	0	0
8	14	NA	NA	NA	NA	NA	NA	NA	NA
9	16	+ –	+ –	90	70	10	0	0	0
10	18	+ –	+ –	80	100	10	0	0	0
11	20	NA	NA	NA	NA	NA	NA	NA	NA

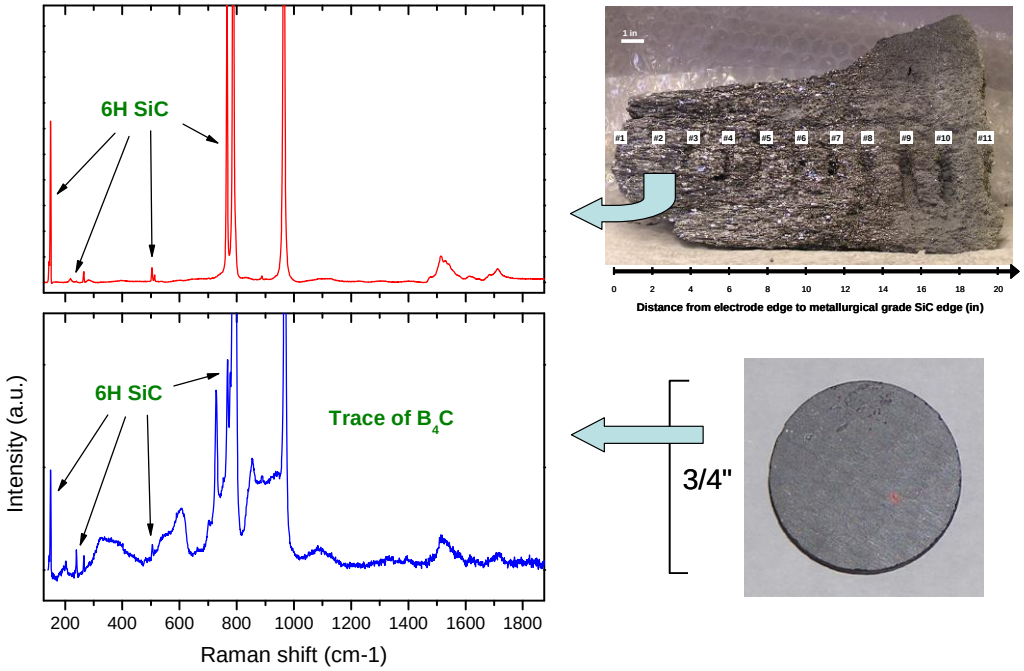

Fig. 3.4 Raman spectra of carbothermically reacted SiC collected from the areas near graphitic electrode: as-received samples (top) and sintered ceramics (bottom). The trace of B_4C is originated from the sintering aids.

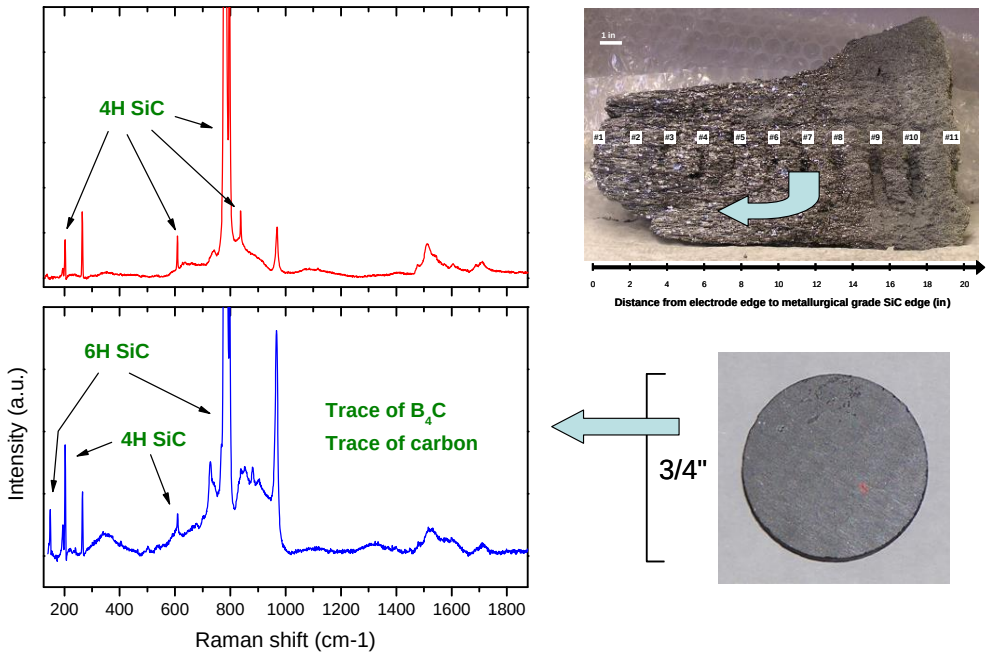

Fig. 3.5 Raman spectra of carbothermically reacted SiC collected from the areas between graphitic electrode and metallurgical-grade edge: as-received samples (top) and sintered ceramics (bottom). The traces of C and B_4C are originated from the sintering aids.

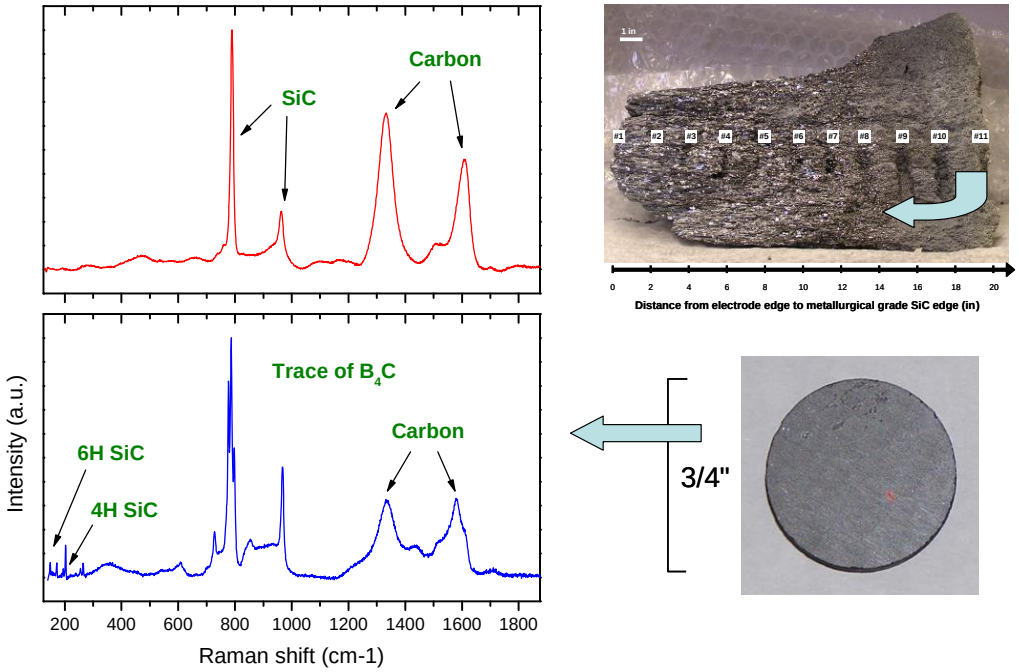

Fig. 3.6 Raman spectra of carbothermically reacted SiC collected from the areas far from graphitic electrode, near metallurgical-grade edge: as-received samples (top) and sintered ceramics (bottom). The traces of C and B_4C are originated from the sintering aids.

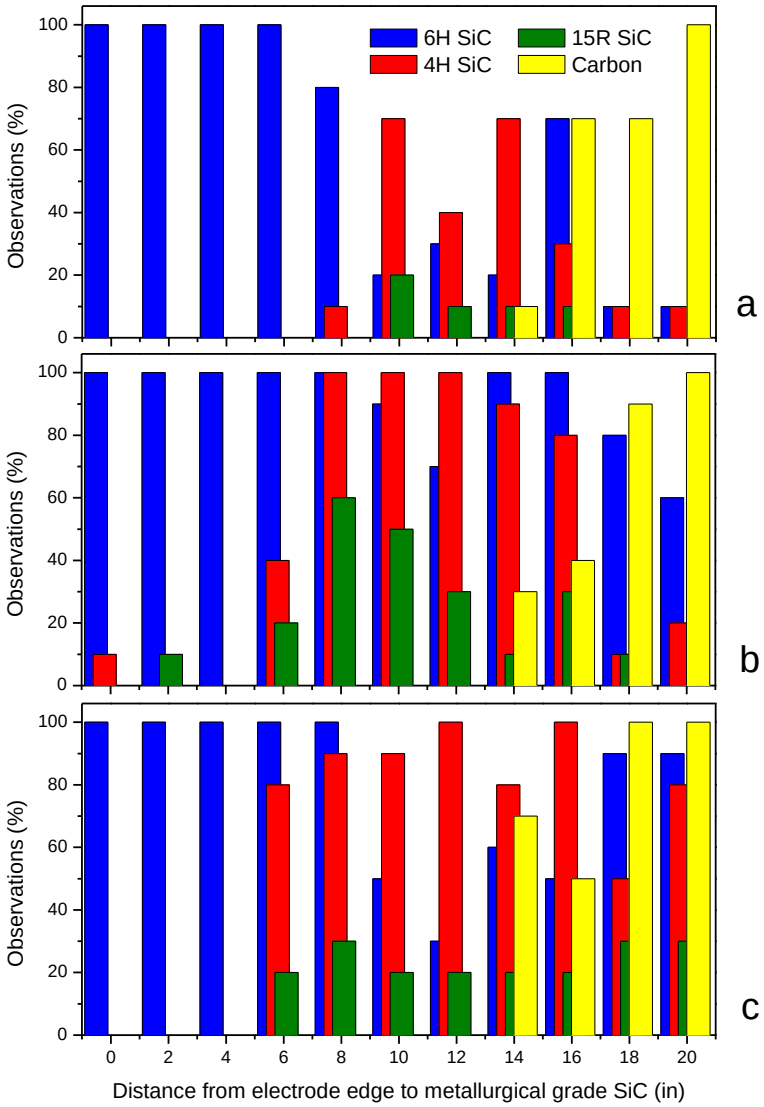

Fig. 3.7 Distribution of selected SiC polytypes and graphitic C content in carbothermically reacted SiC: (a) as-received samples, (b) powders after jet milling, and (c) sintered samples (with sintering aids). Analysis was done based on the number of observation of Raman bands pertaining to a particular SiC polytype/graphitic C.

To evaluate the mechanical properties of the sintered samples, Knoop hardness measurements were carried out. As follows from the data shown in Table 3.6, the density of many sintered samples appeared significantly lower than the theoretical density of SiC (3.21 cm^3). This was found to be a consequence of insufficient milling, as the analyzed powders exhibited multimodal size distribution, with some particles extending into the dimensions of tens of microns (red curves in Fig. 3.8). Repeated (up to 20 times) milling was adopted and density of the powders comminuted using this method to this date is shown in Fig. 3.8 as green curves. The particle distribution of the powders milled repeatedly is centered on 1–2 μm, with

a single-mode distribution. These powders densified to density of approximately 97% ρ_{th} during sintering. As shown in Fig. 3.9, it was possible in most cases to locate highly densified areas even on the generally porous samples, and Knoop indents were placed within these areas for hardness measurements. Homogeneous appearance of the analyzed sample surface, as well as the regular shape of the indents and the absence of extended cracking, all suggest that these data can give a reliable estimate of the hardness of sintered samples corresponding to different areas within the carbothermic reactor. To this date, reliable hardness measurements were not possible only for samples nos. 3 and 5.

Table 3.6 Density and Knoop hardness of sintered samples (with sintering aids)

Sample No.	Density (cm^3)	Relative Density ($\%\rho_{th}$)	Knoop Hardness (kgf/mm^2)
1	3.03	94.4	2,169 ± 70
2	3.14	97.8	2,152 ± 64
3	2.63	81.9	NA
4	3.14	97.8	2,080 ± 59
5	2.91	90.7	NA
6	3.13	97.5	2,067 ± 61
7	3.13	97.5	2,137 ± 85
8	2.86	89.9	2,193 ± 57
9	3.14	97.8	2,098 ± 65
10	3.14	97.8	1,949 ± 51
11	2.78	86.6	1,934 ± 50

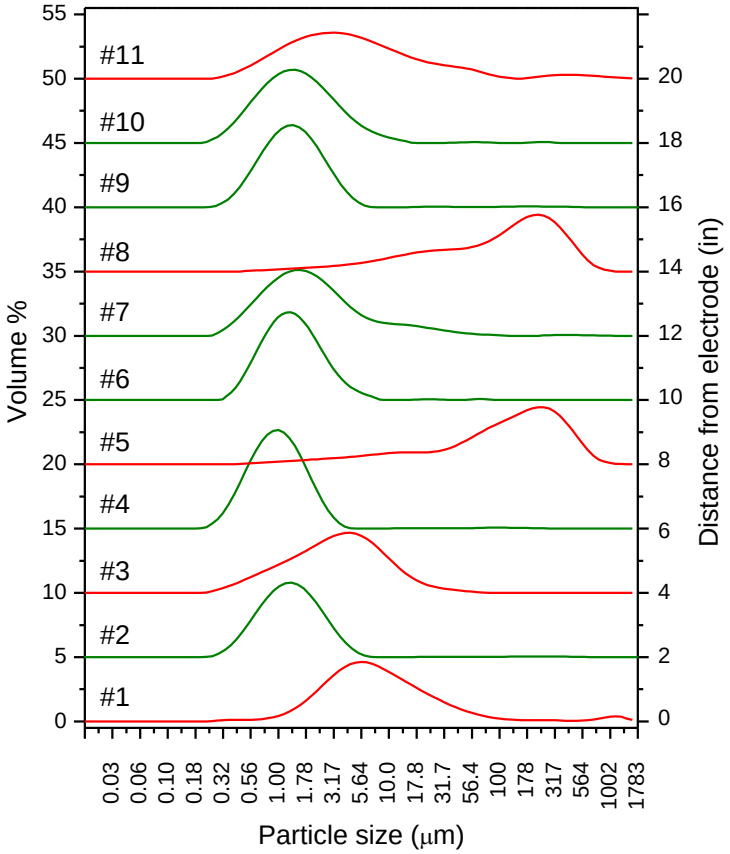

Fig. 3.8 Particle size analysis results for powders 1–11; powders shown in green have been milled over 15 times. The average particle size is near 1 μm for powders subjected to repeated jet milling.

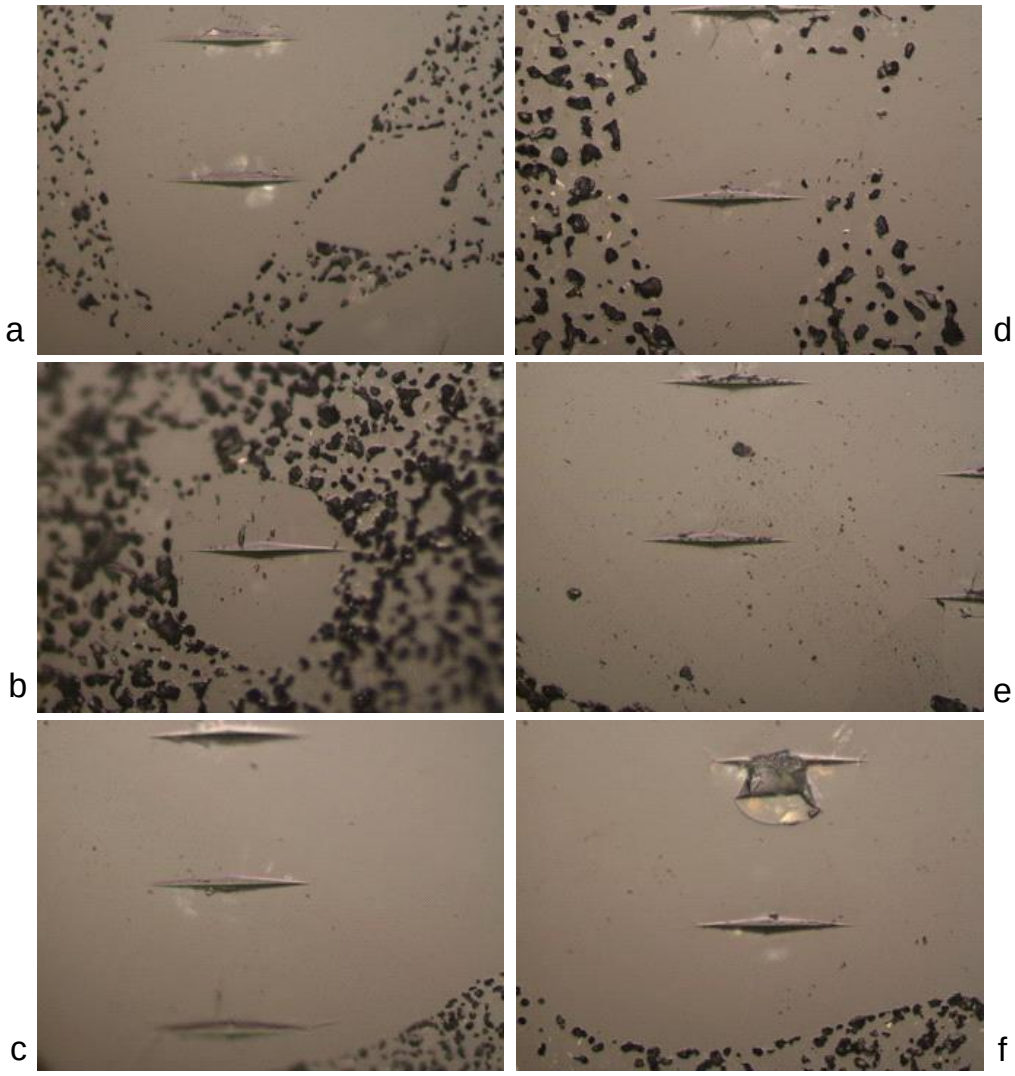

Fig. 3.9 Optical images of Knoop indents in selected sintered samples: (a) 1, (b) 3, (c) 5, (d) 6, (e) 8, and (f) 9. Absence of visible cracking and the regular shape of most indents suggest that selected localized areas in the sintered samples are fully densified.

Densities and 1-kgf Knoop hardness data of selected samples sintered with the use of sintering aids are shown in Fig. 3.10 as a function of the distance from the electrode. These data show correlation with the SiC polytype and C distribution in the same samples shown in Fig. 3.7c.

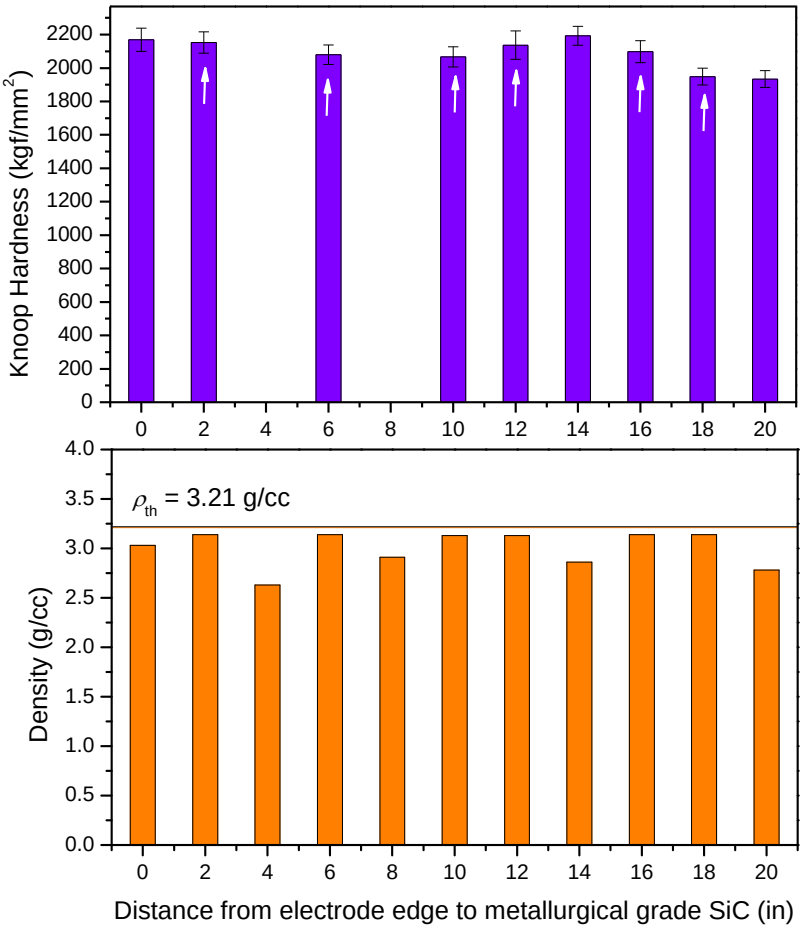

Fig. 3.10 Density (bottom) and 1-kgf Knoop hardness (top) data on samples produced with the use of the sintering aids as a function of the distance from the electrode. Only reliable hardness data has been included. The hardness data marked by white arrows is obtained on samples with density near 97% $\rho_{th.}$

It was established that subjecting powders to repeated jet milling was leading to an improved packing during sintering and resulted in near theoretical density of the sintered material produced without the use of sintering aids. The density and Knoop hardness of the sintered samples 2, 4, 6, 7, 9, and 10 produced without sintering aids are shown in Table 3.7. These data are compared with the composition of the same samples in Fig. 3.11. There appears to be a similar correlation between hardness and SiC polytype composition as the one observed for samples sintered with the use of sintering aids shown in Figs. 3.10 and 3.7. The hardness is highest for samples consisting of 6H SiC polytype and lowest near the metallurgical-grade SiC edge. Formation of the 4H SiC polytype lowers hardness to some extent. One notable difference between Figs. 3.7 and 3.11 is the absence of free C near the metallurgical-grade edge in the samples sintered without the use of sintering aids. This suggests that all free C is reacted in this case. Negligible effect on the hardness of the free C can be explained by the selection of only regularly

shaped indents adopted in this work; apparently these indents were not affected by structural imperfections such as C inclusions. Additional work on comparative measurements of macro-mechanical properties of the samples sintered with and without the use of sintering aids will be required to clarify this issue.

Table 3.7 Density and Knoop hardness of sintered samples (no sintering aids)

Sample No.	Density (cm^3)	Relative Density ($\%\rho_{th}$)	Knoop Hardness (kgf/mm^2)
1	NA	NA	NA
2	3.13	97.5	1,985 ± 64
3	NA	NA	NA
4	3.14	97.8	1,931 ± 52
5	NA	—	NA
6	3.11	96.9	1,964 ± 57
7	3.13	97.5	1,979 ± 59
8	NA	NA	NA
9	3.12	97.2	1,912 ± 54
10	3.14	97.8	1,825 ± 53
11	NA	NA	NA

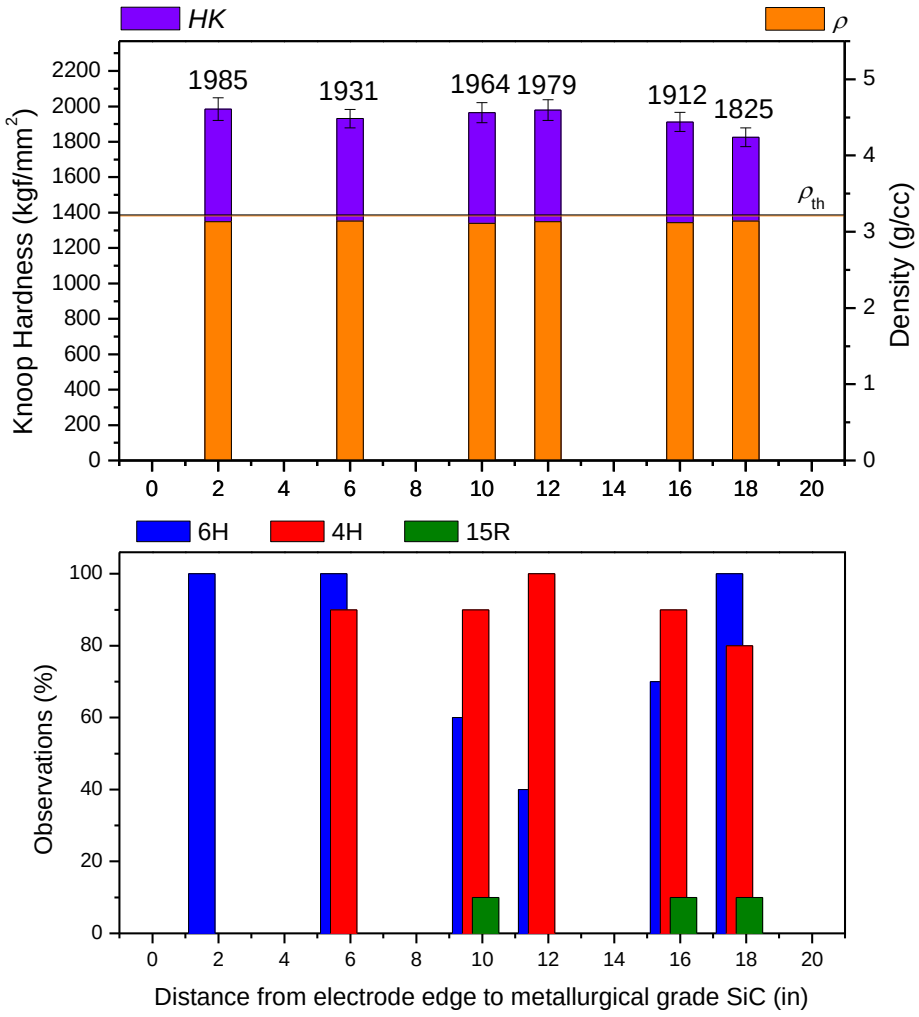

Fig. 3.11 Correlation between hardness (top) and compositions (bottom) for selected SiC samples densified using SPS method without the use of sintering aids. All samples have been sintered to density of approximately 97% ρ_{th}.

The results of chemical analysis of the unprocessed samples are shown in Fig. 3.12 and Table 3.8. The presence of unreacted Si and C, as well as magnesium (Mg), Al, calcium (Ca), titanium (Ti), vanadium (V), iron (Fe), and zirconium (Zr) impurities has been detected in the samples. Increased concentrations of free C were observed near the metallurgical-grade edge, similar to the X-ray diffraction and Raman results. The increased free C content is correlated with the increased concentrations of metal impurities, as shown in Fig. 3.12. Increased concentrations of free Si were observed in the crystalline-grade zone adjacent to the boundary with the metallurgical-grade SiC. However, no direct correlation between the formation of 4H SiC polytype and the presence of metal impurities could be established.

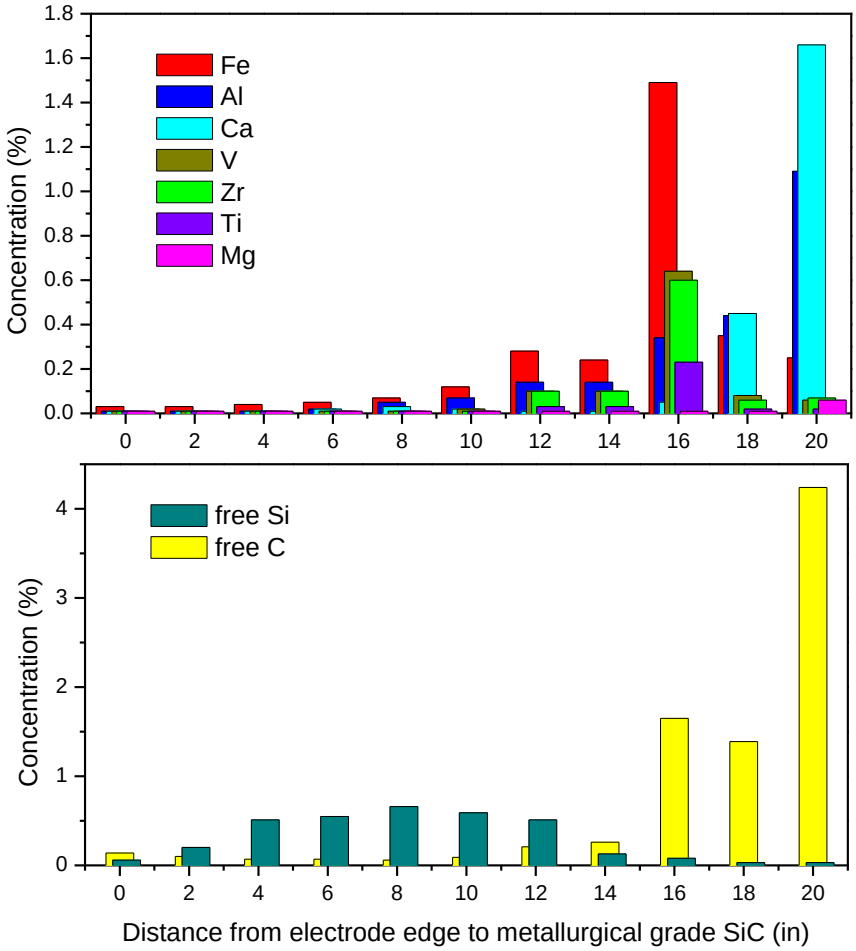

Fig. 3.12 Distribution of metal impurities (top) and unreacted (bottom) C and Si inclusions in carbothermically reduced SiC, as a function of the distance from the graphite electrode

Table 3.8 Summary of the results of chemical analysis of unprocessed carbothermally reduced SiC

Sample No.	Distance from Electrode Edge (inches)	Metallic Impurities (%)							Free C (%)	Free Si (%)
		Mg	Al	Ca	Ti	V	Fe	Zr		
1	0	0.01	<0.01	0.01	<0.01	<0.01	0.03	<0.01	0.06	0.14
2	2	0.01	<0.01	<0.01	<0.01	<0.01	0.03	<0.01	0.20	0.10
3	4	0.01	<0.01	0.01	<0.01	<0.01	0.04	<0.01	0.51	0.07
4	6	0.01	0.02	0.02	<0.01	<0.01	0.05	<0.01	0.55	0.07
5	8	0.01	0.05	0.03	<0.01	<0.01	0.07	<0.01	0.66	0.06
6	10	0.01	0.07	0.02	<0.01	0.02	0.12	<0.01	0.59	0.09
7	12	0.01	0.14	0.01	0.03	0.10	0.28	0.10	0.51	0.21
8	14	0.01	0.14	<0.01	0.03	0.10	0.24	0.10	0.13	0.26
9	16	0.01	0.34	0.05	0.23	0.64	1.49	0.60	0.08	1.65
10	18	0.01	0.44	0.45	0.02	0.08	0.35	0.06	0.03	1.39
11	20	0.06	1.09	1.66	0.02	0.06	0.25	0.07	0.03	4.24

3.5 Future Work

Repeated jet milling will be used for reducing the remaining powders to the size close to 1 μm. Chemical analysis of milled powders will be performed once sufficient quantities of powders have been prepared. Samples representing various zones in the carbothermic reactors will be sintered with and without the use of sintering aids. Additionally, hydrofluoric acid washing will be used for the same powders prior to sintering to remove excess O and metal impurities. Physical and mechanical properties of the sintered samples will be evaluated and correlated with chemistry and polytypism of the starting material.

3.6 References

1. Weimer AW, editor. Carbide, boride, and nitride materials synthesis and processing. London: Chapman and Hall; 1997.
2. Patrick L, Hamilton DR, Choyke WJ. Phys Rev. 1966;143:526.
3. Patrick L. Phys Rev. 1968;167:809.
4. Feldman DW, Parker JH Jr, Choyke WJ, Patrick L. Phys Rev. 1968;170:698.
5. Feldman DW, Parker JH Jr, Choyke WJ, Patrick L. Phys Rev. 1968;173:787.
6. Merlin R, Pinczuk A, Weber WH. Overview of phonon Raman scattering in solids. In: Weber WH, Merlin R., editors. Raman scattering in materials science. New York: Springer; 2000; p. 1–29.
7. Ferrari AC, Robertson J. Phys Rev B. 2000;61:14095.

1 (PDF) DEFENSE TECHNICAL INFORMATION CTR DTIC OCA

2 (PDF) DIRECTOR US ARMY RESEARCH LAB RDRL CIO LL IMAL HRA MAIL & RECORDS MGMT

1 (PDF) GOVT PRINTG OFC A MALHOTRA

45 (7 HC, 38 PDF) DIR USARL
RDRL CIH C
D GROVE
J KNAP
RDRL WM
P BAKER
B FORCH
J MCCAULEY (6 HC, 1 PDF)
P PLOSTINS
RDRL WML B
I BATYREV
B RICE
D TAYLOR
N WEINGARTEN
RDRL WML H
B SCHUSTER
RDRL WMM
J BEATTY
R DOWDING
J ZABINSKI
RDRL WMM B
G GAZONAS
RDRL WMM E
S KILCZEWSKI
J LASALVIA
P PATEL
J SINGH
J SWAB
RDRL WMP
S SCHOENFELD
RDRL WMP A
S BILYK
RDRL WMP B
C HOPPEL
S SATAPATHY
M SCHEIDLER
T WEERASOORIYA
RDRL WMP C
R BECKER
T BJERKE
D CASEM
J CLAYTON (1 HC)
D DANDEKAR
M GREENFIELD
R LEAVY
S SEGLETES
C WILLIAMS
RDRL WMP D
R DONEY
RDRL WMP E
S BARTUS
RDRL WMP F
N GNIAZDOWSKI
RDRL WMS
M VANLANDINGHAM

INTENTIONALLY LEFT BLANK.